Research Square

Preprints are preliminary reports that have not undergone peer review.
They should not be considered conclusive, used to inform clinical practice,
or referenced by the media as validated information.

Viscoelasticity reprograms T cell metabolism for TCR-T cell manufacturing and therapy

Song Li

songli@ucla.edu

University of California, Los Angeles https://orcid.org/0000-0002-4760-8828

Youcheng Yang

University of California, Los Angeles

Yan-Ruide Li

University of California Los Angeles https://orcid.org/0000-0002-9858-300X

Zeyang Liu

University of California, Los Angeles https://orcid.org/0000-0002-3553-3793

Hao Zhou

University of Southern California

Yichen Zhu

University of California Los Angeles

Xinyuan Shen

UCLA https://orcid.org/0009-0002-2788-3993

Dexter Lai

University of California, Los Angeles

Yihui Cen

University of California, Los Angeles

Emily Miller

Terasaki Institute for Biomedical Innovation https://orcid.org/0009-0007-8137-3122

Haochen Nan

University of California, Los Angeles

Bo Zhang

University of California, Los Angeles

Shubing Wang

University of California, Los Angeles

Jason Lin

University of California, Los Angeles

Yuning Chen

University of California, Los Angeles https://orcid.org/0009-0000-8010-670X

Bella Raykowski

University of Southern California

Enbo Zhu

UCLA https://orcid.org/0000-0001-8600-8553

Jun Shen

University of California, Los Angeles

Keyue Shen

University of Southern California https://orcid.org/0000-0001-9605-1635

Junyoung Park

UCLA https://orcid.org/0000-0001-9869-8993

Jingyi Li

University of California, Los Angeles

Xiling Shen

Terasaki Institute for Biomedical Innovation

Zhaohui Wang

Terasaki Institute for Biomedical Innovation

Lili Yang

University of California, Los Angeles https://orcid.org/0000-0001-6568-0404

Article

Keywords: T cell Activation, Viscoelasticity, TCR-T Cell Therapy, T cell metabolism

Posted Date: March 6th, 2026

DOI: https://doi.org/10.21203/rs.3.rs-8855735/v1

License: This work is licensed under a Creative Commons Attribution 4.0 International License.
Read Full License

Additional Declarations: Yes there is potential Competing Interest. L.Y. is a scientific advisor to AlzChem and Amberstone Biosciences, and a co-founder, stockholder, and advisory board member of Appia Bio. None of the declared companies contributed to or directed any of the research reported in this article. The remaining authors declare no competing interests.

Viscoelasticity reprograms T cell metabolism for TCR-T cell manufacturing and therapy

Youcheng Yang[1], Yan-Ruide Li[1,2]*, Zeyang Liu[1]*, Hao Zhou[3,4], Yichen Zhu[1,2], Xinyuan Shen[1,2], Dexter Lai[5], Yihui Cen[6], Emily Miller[7], Haochen Nan[1], Bo Zhang[1], Shubing Wang[1], Jason Lin[1], Yuning Chen[1,2], Bella Raykowski[3], Enbo Zhu[1,2,8], Jun Shen[9], Keyue Shen[3,10], Junyoung O. Park[1,5], Jingyi Jessica Li[6,11], Xiling Shen[7], Zhaohui Wang[7], Lili Yang[1,2,12,13,14]¶, Song Li[1,13,14]¶*

[1] Department of Bioengineering, University of California Los Angeles, Los Angeles, CA 90095, USA

[2] Department of Microbiology, Immunology & Molecular Genetics, University of California Los Angeles, Los Angeles, CA 90095, USA

[3] Alfred E. Mann Department of Biomedical Engineering, University of Southern California, Los Angeles, CA 90089, USA

[4] Eli & Edythe Broad CIRM Center for Regenerative Medicine & Stem Cell Research, University of Southern California, Los Angeles, CA 90033, USA

[5] Department of Chemical and Biomolecular Engineering, University of California Los Angeles, Los Angeles, CA 90095, USA

[6] Department of Computational Medicine, University of California Los Angeles, Los Angeles, CA 90095, USA

[7] Terasaki Institute for Biomedical Innovation, Woodland Hills, CA 91367, USA

[8] Department of Materials Science and Engineering, University of California, Los Angeles, Los Angeles, CA 90095, USA

[9] Department of Chemistry and Biochemistry, University of California Los Angeles, Los Angeles, CA 90095, USA

[10] Norris Comprehensive Cancer Center, University of Southern California, Los Angeles, CA 90033, USA

[11] Biostatistics Program, Public Health Sciences Division, Fred Hutchinson Cancer Center, Seattle, WA 98109, USA

[12] Molecular Biology Institute, University of California Los Angeles, Los Angeles, CA 90095, USA

[13] Eli and Edythe Broad Center of Regenerative Medicine and Stem Cell Research, University of California Los Angeles, Los Angeles, CA 90095, USA

[14] Jonsson Comprehensive Cancer Center, David Geffen School of Medicine, University of California Los Angeles, Los Angeles, CA 90095, USA

* Equal contribution

¶ Corresponding authors: liliyang@ucla.edu (Y.L.); songli@ucla.edu (S.L.)

Keywords: T cell Activation; Viscoelasticity; TCR-T Cell Therapy; T cell metabolism

Abstract

Adoptive T cell receptor (TCR)–based immunotherapy offers a powerful strategy to target solid tumors through recognition of either cell surface antigens or intracellular tumor antigens. However, T-cell activation requires the coordinated integration of biochemical cues and physical properties of the antigen-presenting interface, and the mechanistic basis by which these microenvironmental parameters regulate T-cell metabolic programming remains poorly defined. Here we develop synthetic viscoelastic activating cells (SynVAC)—a class of artificial antigen-presenting cells (aAPCs) whose stress-relaxation kinetics are independently and precisely chemically tuned while maintaining constant stiffness and defined densities of peptide–major histocompatibility complex (pMHC) and co-stimulatory ligands. SynVAC-pMHC offers a well-defined and scalable platform that outperforms monocyte-derived dendritic cells (moDCs) to enrich antigen-specific $CD8^+$ T cells. Particularly, fast-relaxing SynVAC-pMHC amplifies TCR signaling and mTOR activity, drives mitochondrial remodeling, and programs antigen-specific T cells toward an energetically favorable metabolic state with enhanced stem-like properties. Furthermore, TCR-T cells expanded using fast-relaxing SynVAC-pMHC exhibit superior persistence and durable antitumor activity in melanoma and ovarian cancer models. Together, these results establish cell-mimetic viscoelasticity as a key biophysical cue governing T cell metabolism and differentiation, and provide a scalable, fully synthetic strategy to manufacture potent TCR-T cells for solid tumor therapy.

Introduction

T cell receptor-modified T (TCR-T) cell therapy offers a powerful strategy to target solid tumors by recognizing both cell surface antigens and intracellular tumor antigens presented by MHC[1]. This innovative treatment begins by extracting T cells from a patient's blood and modifying their TCRs or expanding certain T cell populations that recognize and attack cancer cells with specific antigens, such as NY-ESO-1, MAGE-A3, and MART-1[2,3]. Nevertheless, existing TCR-T manufacturing platforms continue to encounter significant challenges. For example, monocyte-derived dendritic cells (moDCs) are commonly used for antigen-specific T cell activation; however, they exhibit limited fidelity to naturally circulating dendritic cell subsets and are typically generated under inflammatory conditions that may not recapitulate native antigen presentation. Consequently, moDC-based expansion is associated with suboptimal *in vitro* proliferation, accelerated phenotypic exhaustion, and limited *in vivo* persistence following infusion, in addition to donor-to-donor variability, poor scalability, and poorly controlled paracrine signaling[4,5].

Another widely used *in vitro* T cell activation method prior to TCR modification, stimulation with polystyrene beads coated with anti-CD3/CD28 antibodies or human leukocyte antigen–immunoglobulin fusion protein (HLA-Ig) and CD28-specific antibody, often triggers excessive stimulation, rapid T cell differentiation, and low T memory stem cells (TMSCs)[6-9]. To address these challenges, there is a critical need to develop next-generation aAPCs that not only deliver precise antigenic and costimulatory cues but also mimic the biophysical context of natural antigen presentation. Such platforms may enable the expansion of metabolically fit, memory-enriched T cells with improved persistence and tumor-clearing potential, thereby advancing the efficacy of TCR-T cell therapy against solid tumors.

Mechanical cues represent a fundamental but often underappreciated dimension of immune regulation, complementing the well-established roles of biochemical and cytokine-mediated signaling[10-12]. In T cells, mechanotransduction through TCR at the immune synapse regulates activation strength, cytokine secretion, and killing potency[13-18]. Notably, the stiffness of aAPCs within the physiological range of 1-30 kPa has been shown to optimize T cell activation and expansion[19-23]. In addition, the viscoelasticity of aAPCs or ECM, when using anti-CD3/CD28 as activation signals, enhances the stemness of expanded T cells[24,25]. However, the mechanisms by which viscoelastic cues influence T cell fate remain poorly understood. In parallel, accumulating evidence suggests that the metabolic fitness of T cells—including mitochondrial function, oxidative phosphorylation capacity, and balanced glycolytic activity—is a critical

determinant of T cell differentiation and sustained antitumor immunity[26,27]. Whether and how the viscoelastic properties of antigen-presenting materials regulate T cell metabolic programming and differentiation remains an open question.

To better replicate the physiological cues of natural APCs, here we develop SynVAC-pMHC with tunable stress-relaxation kinetics, which recapitulates the mechanical properties of natural APCs while presenting precisely defined pMHC and costimulatory ligands for antigen-specific TCR engagement. We find that fast-relaxing SynVAC-pMHC outperforms moDCs in promoting T cell expansion and memory enrichment of antigen-specific $CD8^+$ T cells through a mechanism of metabolic reprogramming. TCR-engineered T cells expanded on fast-relaxing SynVAC-pMHC exhibit durable *in vivo* persistence and superior antitumor efficacy across multiple solid tumor models. These findings establish viscoelasticity as a key biophysical regulator of TCR-driven T cell fate and position SynVAC-pMHC as a physiologically relevant, scalable platform for manufacturing potent TCR-T cell therapies.

Results

Fabrication of SynVAC-pMHC with tunable viscoelasticity

In previous studies, we have demonstrated that the viscoelastic properties of SynVAC coated with activating antibodies promote T-cell stemness and durability, and that a stiffness of 10 kPa is superior to 30 kPa[24]. Based on these findings, we designed a panel of SynVAC–pMHC constructs with varying stress-relaxation times while maintaining constant stiffness (10 kPa) and ligand density (Figure 1a). These SynVAC-pMHC were used to investigate how mechanical relaxation influences antigen-specific T cell activation and function. In brief, four formulations of alginate-based microbeads (V1–V4) were engineered to exhibit half stress-relaxation times ranging from ~10 to ~700 seconds (Extended figure 1a)**.** This mechanical property was measured by using disc-shaped hydrogels (8 mm diameter, 2 mm thick) corresponding to each SynVAC-pMHC formulation and subjecting them to compressive mechanical testing. Atomic force microscopy (AFM) was further used to confirm their difference in viscoelasticity in the microbead formulation (Extended figure 1b). Furthermore, we confirmed that all formulations exhibited comparable stiffness (~5 kPa), ensuring that differences among groups arose solely from variations in stress relaxation (Extended figure 1c). This design allowed us to isolate the effect of viscoelasticity on T cell activation dynamics.

Surface functionalization was performed using EDC/NHS chemistry to activate carboxyl groups on the alginate matrix, enabling conjugation of trans-cyclooctene (TCO) moieties.

Subsequent click chemistry allowed for the attachment of tetrameric HLA-A*02:01/NY-ESO-1 (pMHC) and anti-CD28 antibodies to the bead surface, facilitating antigen-specific T cell stimulation. This strategy was chosen for its high specificity and biocompatibility to covalently anchor tetrameric HLA-A*02:01/NY-ESO-1 complexes and anti-CD28 antibodies onto the bead surface.

To investigate the influence of viscoelasticity on antigen-specific T cell activation, SynVAC-pMHC (V1–V4) were cocultured with human peripheral blood mononuclear cells (PBMCs) pre-screened for HLA-A2 positivity. Flow cytometry at day 14 revealed that V1–V3 supported similar levels of NY-ESO-1-specific T (ESO-T) cell expansion, while V4 significantly underperformed in both metrics (Extended figure 1d,e). Furthermore, the *in vitro* tumor killing assays also showed that V4-expanded cells have significantly less tumor killing ability with tumor cell lines OVCAR3 and A375 (Extended figure 1f,g). Accordingly, we selected V1 (fast-relaxing) and V4 (medium-relaxing) for further experimentation, alongside a slow-relaxing formulation (2000s half-relaxation time) and a control group utilizing moDCs. These SynVAC-pMHC were denoted as fast-relaxing beads (FRB), medium-relaxing beads (MRB), and slow-relaxing beads (SRB). Their 50% half-relaxation time was shown in Figure 1b. For simplicity, the abbreviations FRB, MRB, and SRB are used throughout the text.

Characterization of SynVAC-pMHC viscoelasticity and surface properties

To ensure that stiffness was not a confounding factor, AFM was used to measure the stiffness of FRB, MRB, and SRB, confirming uniformity across all groups (Figure 1c). To further corroborate these findings, bulk gel analogs were also analyzed using a rheometer, which demonstrated FRBs displayed higher loss modulus (G") (Figure 1d) and tan δ (Figure 1e) compared to MRBs and SRBs across tested frequencies, supporting their enhanced viscoelasticity.

To assess ligand density and distribution, flow cytometry was performed, showing consistent conjugation efficiency across all SynVAC-pMHC types (Figure 1f). Confocal imaging further confirmed that ligand attachment was localized uniformly to the bead surface, optimizing antigen presentation and cost-efficiency (Figure 1g). Additionally, X-ray photoelectron spectroscopy (XPS) indicated similar calcium content in FRB and MRB beads, while SRB lacked calcium, reflecting its altered crosslinking profile (Figure 1h).

Interaction of SynVAC-pMHC with ESO-T cells and activation potency

To visualize the initial physical interactions between antigen-specific T cells and SynVAC-pMHC, sorted ESO-T cells derived from human PBMCs were cocultured with FRB for one

hour and analyzed using scanning electron microscopy (SEM). It revealed a close membrane contact and the formation of synapse-like structures between ESO-T cells and FRB, suggesting productive antigen recognition and engagement at the cell–bead interface (Supplementary Figure 1). The morphological features of these contacts—such as membrane spreading, polarization, and tight junction formation—resemble the early stages of an immunological synapse, a hallmark of TCR-mediated recognition events.

To further assess the functional outcome of these early interactions, we measured the expression of the early activation marker CD69 following short-term coculture (Figure 1i). CD69 is rapidly upregulated upon TCR engagement and serves as a sensitive indicator of proximal signaling events within the first few hours of antigen recognition. Compared to MRBs and SRBs, which possess reduced viscoelasticity, FRBs induced markedly higher levels of CD69 expression (Figure 1j). This enhanced activation suggests that both the mechanical properties and the biochemical ligand presentation of FRBs synergize to potentiate early T cell signaling.

Together, these results indicate that the viscoelastic nature of FRBs not only facilitates stable synapse formation but also promotes more efficient initiation of T cell activation.

Antigen-specific expansion of human primary PBMCs by SynVAC-pMHC

To investigate whether mechanical relaxation of SynVAC-pMHC regulates antigen-specific T cell responses, we performed *in vitro* expansion experiments using SynVAC-pMHC with distinct viscoelastic relaxation times. PBMCs from HLA-A2-positive donors were activated using FRB, MRB, SRB, or moDCs at a 1:1 ratio, followed by restimulation on day 7 and functional assessment on day 14 (Figure 2a). Consistent with prior results, FACS analysis showed that FRBs drove significantly higher ESO-T cell frequency (Figure 2b,c) and expansion (Figure 2d) than MRBs or SRBs on day 14, suggesting that the presentation of pMHC with fast relaxation promotes T cell proliferation and/or survival. To assess functional cytotoxicity, ESO-T cells expanded under each condition were co-cultured with HLA-A2/NY-ESO-1 positive melanoma (A375-FG) or ovarian (OVCAR3-FG) tumor targets for 24 hours (Figure 2e). The result showed superior tumor-killing efficiency in the FRB group (Figure 2f, g). Cytokine analysis via ELISA further confirmed this trend: FRB-expanded T cells secreted higher levels of IFN-γ, TNF-α, and IL-2 (Figure 2h–j), suggesting enhanced killing capability. Furthermore, T cell and tumor organoid co-culture indicated a superior infiltration capability, with the FRB resulting in the greatest T cell infiltration into the organoids compared to MRB, SRB, and control conditions (Figure 2k, l).

These results demonstrate that modulating the viscoelastic properties of SynVAC-pMHC can substantially affect antigen-specific T cell expansion, effector function, and cytokine secretion *in vitro*. Furthermore, we found that MRB performs similarly to SRB, suggesting an optimal range of the SynVAC-pMHC viscoelasticity around 10 sec (FRB).

scRNA-seq analysis of expanded T cell populations

To examine how mechanical relaxation of SynVAC-pMHC affects long-term T cell differentiation and clonal architecture, we performed single-cell RNA and TCR sequencing on ESO-T cells expanded by FRB and SRB, alongside moDCs as the benchmark for antigen-specific activation, using the 10X Genomics platform at day 14. Following alignment with CellRanger (V9.0.0), downstream analysis was performed in Seurat (v4.3.0). To ensure that UMAP's 2D embeddings reliably inform the similarities among cell clusters, scDEED (v0.1.0) was used to optimize the UMAP hyperparameters and minimize the number of dubious cell embeddings[28]. The UMAP visualization revealed eight distinct clusters (Figure 3a), which were annotated based on gene expression profiles in stemness, proliferation, residency, effector, and exhaustion (Figure 3b).

As shown in Figure 3b, FRB-expanded ESO-T cells had more T memory stem (cluster 1 in 3a) and T central memory (cluster 2 in 3a) subsets. In contrast, SRB- and moDC-expanded cells exhibited higher proportions of exhausted cells (cluster 7,8) and terminally differentiated T cells (cluster 5) (Supplementary Figure 2). Heatmap projection of CCR7, TCF7, and SELL expressions further confirmed elevated stemness-related gene expression in FRB-expanded cells (Figure 3c, Supplementary Figure 3), along with decreased expression of exhaustion-related markers like PDCD1, LAG3, and TIGIT.

Gene ontology analysis using the fgsea packages[29] and GOBP[30,31] revealed that cell proliferation-related pathways (e.g., Cell Cycle, Cell Cycle Process) were significantly upregulated in FRB-expanded cells (Figure 3d), corroborating their robust expansion profile. Using the Pathway Interaction Database, we found an increased expression of TCR pathway-related genes in the FRB group (Extended Figure 2a). We also observed an upregulation of oxidative phosphorylation-related genes and a downregulation of glycolysis-related genes in the FRB group, consistent with the increased memory stem cell percentage (Extended Figure 2b-c).

Parallel TCR sequencing revealed that TRAV19-TRBV21 and TRAV38-TRBV2 were the most common αβ TCR combinations across all three groups, with the overall TCR combination profiles exhibiting a high degree of similarity (Figure 3e). Despite this overall profile similarity,

the FRB-activated T cells displayed a greater number of unique clones (Figure 3f), and their dominant clones occupied significantly larger proportions of the total population compared to the moDC group (Figure 3g).

Overall, our single-cell analysis demonstrates that the mechanical environment is a critical determinant of T cell fate. The FRB-expanded T cells retained stemness characteristics, showed robust proliferative capacity, and avoided the terminal exhaustion pathways observed in both the SRB and moDC groups. FRB-activated cells also achieved more unique clones, but with a highly focused expansion. These integrated findings confirm that utilizing SynVAC-pMHC (FRB) with a high viscoelasticity can be used to generate antigen-specific T cells optimized for persistence.

Intracellular signaling of ESO-T cells activated by SynVAC-pMHC

To understand how high and low viscoelasticity influences TCR proximal signaling, we examined the formation of the immunological synapse, a critical structure for T cell activation[32,33]. At 15 minutes post-stimulation, SRB induced a more prominent initial immunological synapse compared to FRB (Figure 4a). At 30 and 60 minutes, FRB-mediated synapses remained, while SRB-induced synapses disappeared (Figure 4a). These findings indicate that FRB promotes more stable immunological synapse formation compared to SRB, which likely enhances T cell activation.

To evaluate early T cell activation responses, we performed Western Blotting analysis of ESO-T cells 60 min post-activation. The results showed that phosphorylation of IKBα, NFκB, and c-Jun was enhanced in the FRB-activated group (Extended figure 3a), suggesting an increase in NFκB and AP-1 activation. To further validate our result, we performed bulk RNA sequencing on NY-ESO-1–specific TCR-T cells (ESO-T) 6 hours and 24 hours after stimulation with SynVAC-pMHC (FRB versus SRB). Reads were aligned using STAR (v2.7.11b) and analyzed with DESeq2[34], with Clipper being used to control the false discovery rate (FDR) when comparing differentially expressed genes between FRB and SRB[35]. Initial PCA analysis indicated that FRB, SRB, and the control group are in different locations on the PC1 and PC2 axes, suggesting distinct transcriptomes at both 6 hours and 24 hours post-activation (Extended figure 3b).

Consistently, Gene Set Enrichment Analysis (GSEA), performed using the Pathway Interaction Database and 6-hour post-activation RNA-seq data[29,36], revealed that key TCR downstream pathways—including NFAT, NF-κB, AP-1, and CD8 signaling—were enriched in FRB-activated cells (Figure 4b). We also assessed the top upregulated genes and downregulated

genes between the FRB and SRB groups, and found that the SRB expression pattern is between FRB and control (Extended figure 3c). These results suggest that FRB more effectively activates ESO-T cells at both the transcriptional and translational levels.

Following the enhanced signals, at 24 hours post-activation, FRB-stimulated cells showed an upregulation of genes associated with metabolism (e.g., VDAC1, SCD, HK2) and cell cycle progression (e.g., NSD2, TYMS, CDK2), alongside downregulation of naïve T cell–associated genes (e.g., TCF7, IL7R, KLF2) (Extended figure 3d). GSEA analysis with the hallmark gene sets further confirmed upregulation of glycolysis and oxidative phosphorylation-related genes in the FRB group (Extended figure 3f). Pathway interaction maps based on Gene Ontology Biological Processes (GOBP) showed that FRB-stimulated cells were enriched for mitochondrial metabolism, oxidative phosphorylation, and ribosome biogenesis, reflecting a metabolically active and proliferative state (Figure 4c). Additional upregulated pathways included mRNA processing, DNA replication and repair, and telomere maintenance, suggesting coordinated activation of transcriptional and translational machinery to support early activation and memory potential. Consistently, the most enriched pathways at 24 hours include DNA repair and proliferation pathways (Extended figure 3g), such as ATR, FANCONI, and PLK1 signaling, in the FRB group. These results indicated a heightened proliferative potential in the high viscoelasticity SynVAC-pMHC group, aligning with previously described results supporting T cell expansion.

Costimulatory molecules such as CD28 are also a critical component of the immunological synapses, which have been shown to enhance the mTOR activity in T cells[37,38]. The mTOR pathway is a central regulator of T cell metabolism. Among its two functional complexes, mTORC1 promotes glycolytic metabolism, whereas mTORC2 supports mitochondrial oxidative metabolism, including oxidative phosphorylation (OXPHOS)[39,40]. To assess whether the more persistent FRB-induced synapses corresponded to stronger mTOR activity, we measured phosphorylated 4EBP1 (p-4EBP1) and AKT (p-AKT) via confocal microscopy, as readouts for mTORC1 and mTORC2 activity, respectively. FRB-activated T cells exhibited higher levels of both p-4EBP1 and p-AKT compared to MRB or SRB conditions (Figure 4d). Transcription factor targets analysis on the RNA sequencing result also indicated higher activity of mTOR-regulated factors in the FRB-treated group (Extended figure 3e).

To determine whether mTOR signaling mediated the enhanced T cell stemness, we applied rapamycin during the coculture period, which inhibited both mTORC1 and mTORC2 activity (Extended figure 3h). This leads to impaired T cell metabolism (Extended figure 3i), reduced T cell expansion, and reduced generation of TMSCs (Figure 4e,f). These results demonstrate that

mTOR signaling is critical for the FRB-induced enhancement of T cell activation, proliferation, and differentiation.

Metabolism reprogramming of ESO-T cells following activation by SynVAC-pMHC

At the transcriptional level, GSEA of the 24-hour sequencing showed enriched OXPHOS and glycolysis-related genes (Extended figure 3f). To further validate whether FRB-induced activation enhances T cell bioenergetics, we performed a series of analyses on the metabolic activity of ESO-T cells stimulated with FRBs 48 hours post-activation.

At 48 hours post-activation, we observed an increase in cell size in the FRB group compared to other formulations of SynVAC-pMHC (Extended figure 4a), which is often related to a metabolic switch to glycolysis to support T cell growth and proliferation[41,42]. To quantify the metabolic rate of the SynVAC-pMHC-activated cells, the Seahorse XF assay was used to measure the rate of OXPHOS and glycolysis (Figure 5a). FRB-stimulated ESO-T cells exhibited significantly higher basal and maximal oxygen consumption rates (OCR) and elevated extracellular acidification rates (ECAR) compared to MRB- and SRB-stimulated cells (Figure 5b), indicating enhanced mitochondrial respiration and aerobic glycolysis (Figure 5c). This phenomenon was further confirmed in other donors, showing a more energetic metabolism profile in the FRB group (Extended Figure 4b-d). LC-MS metabolomics further revealed increased intracellular lactate, TCA metabolites, redox cofactors, and nucleotide levels in FRB-expanded cells, consistent with higher energy turnover (Figure 5d, Extended Figure 4e).

To visualize metabolic activity at the single-cell level, label-free fluorescence lifetime imaging microscopy (FLIM) was used to measure NAD(P)H intensity and optical redox ratios (i.e. FAD/NAD(P)H)[43]. FRB-activated T cells displayed elevated NAD(P)H signal and lower redox ratios, indicative of a metabolically active state with enhanced biosynthetic potential and upregulation of glycolysis (Figure 5e,f). Consistently, we observed an increased cell size in the FRB group during imaging (Extended figure 4f). We then integrated multiple FLIM-derived metabolic features—including cell morphology, and NAD(P)H lifetimes, intensity, redox ratio, and subcellular distribution—into a 2D metabolic activation map to characterize T cell phenotype[44] (Extended figure 4g). In this analysis, FRB-stimulated cells clustered more tightly in a region representing high mitochondrial activity, whereas SRB- and control-stimulated cells were more dispersed and occupied regions associated with lower metabolic activity (Figure 5g). This suggests that FRB stimulation elicits a more uniform and robust metabolic activation program at the single-cell level, whereas MRB- and SRB-activated cells exhibit less metabolic activity.

Mitochondrial fusion, fission, and biogenesis have also been shown to regulate T cell activation, survival, memory formation, and effector differentiation[45]. To comprehensively assess the metabolic state of the T cells, we evaluated mitochondrial fitness by performing confocal imaging and utilizing MitoTracker Green (for mitochondrial mass) and TMRM (for membrane potential) staining (Figure 5h). The results indicated that FRB-expanded T cells exhibited increased mitochondrial mass (Figure 5i) and a higher mitochondrial membrane potential (Figure 5j) compared to the SRB group, suggesting enhanced mitochondrial activity. To further characterize these changes, we used transmission electron microscopy (TEM) to examine individual mitochondrial structures (Figure 5k). TEM images revealed that mitochondria in the FRB group possessed a greater density of cristae (Figure 5l) and were significantly larger (Figure 5m), which are critical for maximizing the surface area available for oxidative phosphorylation. These results indicate that FRB-activated ESO-T cells have healthier and more functionally robust mitochondria.

Together, these findings support the hypothesis that viscoelasticity is a key regulator of early T cell metabolic programming, with fast stress relaxation enhancing mitochondrial function, OXPHOS, and glycolytic activity, forming a more active metabolic state. Furthermore, we found that MRB-and SRB-activated cells are similar in OXPHOS rate and glycolysis rate, suggesting that there is an optimal viscoelasticity range for T cell metabolism reprogramming.

ESO-T cells expanded with FRB demonstrate superior antitumor capacity in multiple solid tumor xenograft mouse models

To evaluate the translational potential of viscoelastic stimulation, we selected the FRB, which exhibited optimal T cell activation and metabolic fitness *in vitro*, and compared it with the moDC group, the current gold standard for antigen-specific T cell expansion. We assessed the *in vivo* antitumor efficacy of ESO-T cells generated under these two conditions using two solid tumor xenograft models: the OVCAR3-FG human ovarian cancer model and the A375-FG human melanoma model. In the OVCAR3-FG model, tumor cells were injected intraperitoneally (i.p.) into NSG mice to establish a peritoneal tumor burden, mimicking a localized peritoneal disease setting (Fig. 6a). In contrast, A375-FG cells were injected subcutaneously (s.c.) to form solid tumors, allowing assessment of the tumor-homing capacity and antitumor efficacy of ESO-T cells in a solid tumor context (Figure 6h).

In OVCAR3-FG humanized mouse model, ESO-T cells expanded by using FRB or moDCs suppressed tumor growth (Figure 6b,c). However, ESO-T cells generated with FRB exhibited markedly superior antitumor activity, leading to complete tumor elimination in all experimental

mice (Figure 6b,c). Biodistribution and phenotypic analyses of ESO-T cells across multiple organs revealed enhanced *in vivo* persistence, expansion, and preferential peritoneal (tumor site) accumulation (Figure 6d,f). Furthermore, these cells showed enrichment of ESO-specific (ESO^+) T cells, suggesting antigen-specific expansion following tumor encounter (Figure 6e,g). They also expressed elevated levels of T cell activation markers (i.e., PD-1) (Figure 6e,g).

In A375-FG human melanoma xenograft model, the two types of ESO-T cells were also evaluated (Figure 6h). Consistent with the results from the OVCAR3-FG model, ESO-T cells generated with FRB achieved complete tumor elimination in all treated mice, demonstrating significantly higher efficacy compared to those expanded using moDCs (Figure 6i,j). This superior antitumor activity may be attributed to enhanced tumor homing, greater *in vivo* expansion of ESO-T cells observed across multiple tissues (including blood and spleen) (Figure 6k, Supplementary Figure 4), and the enrichment of ESO-T cells with increased expression of the activation marker CD69 (Figure 6l, Supplementary Figure 5).

Collectively, these findings indicate that ESO-T cells expanded using FRB possess superior *in vivo* persistence, tumor-homing capacity, and antitumor efficacy, highlighting their promise as a potent cell product for solid tumor immunotherapy.

Discussion

This study introduces SynVAC-pMHC as a novel, clinically viable platform for the efficient expansion and functional programming of antigen-specific TCR-T cells. SynVAC-pMHC allows for precise control of the mechanical and biochemical signals necessary for T cell activation. We engineered these materials by manipulating the molecular weight and degree of crosslinking to create microparticles with a consistent stiffness of 10 kPa—similar to the stiffness of mature dendritic cells[46]—but widely varying half-relaxation times, ranging from 10 to 2,000 seconds. This capability allows systematic exploration of how material viscoelasticity influences T cell activation and expansion, addressing a key limitation of existing biocompatible materials, which are typically highly elastic and poorly mimic the viscoelastic behavior of native antigen-presenting cells.

In both *in vitro* and *in vivo* studies, we have shown that SynVAC-pMHC can replace and outperform moDCs for TCR-T cell manufacturing. moDCs represent the current standard for TCR-T expansion but suffer from donor variability, phenotypical difference from naturally circulating DC subsets, and are typically generated using GM-CSF/IL-4 that may not recapitulate native APC function[4,5]. SynVAC-pMHC represents a consistent and scalable aAPC platform that provides a bottom-up approach to deliver well-defined signals, avoiding

the mixed and undefined cues associated with moDCs, while uniquely integrating biomechanical modulation to drive metabolic reprogramming for more efficient TCR-T cell expansion.

The most important finding of this work is that the viscoelasticity of the SynVAC-pMHC reprograms the metabolic state of the activated T cells. Upon antigen recognition, naive T cells undergo rapid and dramatic metabolic reprogramming, shifting from quiescent mitochondrial OXPHOS to high-flux aerobic glycolysis. This switch, known as the Warburg effect, is to meet the high energy and biosynthetic demands required for proliferation and effector function[47]. We reveal that FRB, the SynVAC-pMHC with higher viscoelasticity, more effectively drives antigen-specific activation, enhancing intracellular signaling of T cells, including the mTOR pathway. This enhanced signaling elevates both OXPHOS and glycolysis at 48 hours post activation, resulting in more efficient T cell expansion. In contrast, a lower rate of OXPHOS and glycolysis was found in the SRB group, along with lower mitochondrial number and potential, resulting in more exhausted cells[48] at day 14. Furthermore, this energetic T cell metabolism state is linked to an elevated TMSC population, which contributes to their persistence *in vivo* in the mouse xenograft model. These findings, for the first time, establish viscoelasticity as a key biophysical cue that couples mechanosensing to metabolic control in TCR-T cells.

Furthermore, our studies provide mechanistic insight into how the viscoelasticity of aAPCs directly shapes metabolic pathways in T cells. Here we show that fast-relaxing SynVAC-pMHC forms more persistent immune synapses with T cells, and induces higher AP-1, NFκB, NFAT, and mTOR activities in T cells at 15 min to 6 hours post T cell activation. Consistently, higher metabolism and proliferation were observed at 24 hours post-activation. Inhibition of the mTOR pathways suppresses the effect of SynVAC-pMHC with fast relaxation, demonstrating the role of mTOR in mediating viscoelasticity-induced reprogramming of T cell metabolism and TMSC formation. In contrast, previous studies have shown that inhibition of mTOR using RAPA can increase stemness and memory phenotype in the population[49-51]. Unlike these studies, which continued RAPA treatment throughout T cell differentiation, our experiments included RAPA only during the activation phase with SynVAC-pMHC coculture. This discrepancy suggests that elevated mTOR activity during the T cell activation phase, followed by reduced mTOR activity during the differentiation phase, may favor TMSC formation.

In conclusion, we reveal that the viscoelasticity of SynVAC-pMHC is a critical regulator of T cell metabolism, and demonstrate the strong potential of SynVAC-pMHC to enhance TCR T-

cell activation, expansion, and antitumor efficacy. Our findings highlight the advantages of SynVAC-pMHC over conventional moDCs and support their utility as a next-generation platform to overcome key barriers in solid tumor immunotherapy, ultimately paving the way for more effective and durable TCR T-cell treatments in patients with ovarian cancer, melanoma, and beyond.

Methods

Fabrication of the synthetic cells with well-defined mechanical properties

Alginate viscoelastic microbeads were fabricated within the microfluidic device via a pH-induced internal gelation method as previously described [52]. Simply, Polydimethylsiloxane (PDMS) pre-polymer and curing agent were mixed, poured onto the designed silicon substrate, and cured at 65 °C for 3 hours to produce a PDMS slab, followed by ethanol cleaning and plasma treatment for binding to a glass slide. The core stream was loaded with the water phase with different formulations for different viscoelastic microbeads. For FRB, 3% VLVG (MW 70 kD, NovaMatrix), 1% carboxymethyl cellulose (90 kD, Sigma Aldrich), and 20mM Ca-EDTA in deionized (DI) water were used. For MRB, 3% LVG (Sigma Aldrich), 1% MVG (Sigma Aldrich), and 20mM Ca-EDTA in deionized (DI) water were used. The oil phase contained 1% surfactant (157 FSH, Krytox), and 0.5% acetic acid, all dissolved in fluorocarbon oil (Novec 7500, 3M). Both fluids, sterilized with a 0.22-micron filter before use, were connected to the microfluidic device via separate inlets, facilitated by syringe pumps (Harvard Apparatus). The bead-oil mixture was collected into a new tube containing 10% perfluoro-1-octanol (PFO) (Sigma) and 0.2% acetic acid in fluorocarbon oil, which promoted crosslinking. Subsequently, HEPES buffer (with 2 mM calcium chloride, pH=7.2) was added to the collection tube. The tube was centrifuged at 1500g for 1.5 minutes to transition the microbeads from the oil phase to the HEPES buffer.

SRB were fabricated by converting ionically crosslinked viscoelastic microbeads into permanently crosslinked covalent microbeads. Microbeads made with VLVG were centrifuged at 6000g for 5min, and resuspended in MES-Ca buffer (with 1 mM calcium chloride, pH=6) to adjust the pH to 6. Subsequently, the microbeads were centrifuged again and resuspended in MES-Ca buffer containing 50mg/ml 1-Ethyl-3-(3-dimethyl aminopropyl) carbodiimide (EDC), 3.5mg/ml hydroxy benzotriazole (HoBt), and 0.52mg/ml adipic acid dihydrazide (AAD) for overnight incubation. Finally, a sodium citrate buffer (77 mM NaCl, 55 mM sodium citrate) was introduced to the elastic beads for 2 hours to chelate calcium ions and completely remove

the ionic crosslink bonds. The covalent beads were then rinsed with HEPES-T buffer (HEPES buffer with 0.5% Tween20) and stored at 4 ℃ for future use.

Preparation of synthetic cells for T cell stimulation

Synthetic cells are conjugated with human MHC (HLA-A2-NY-ESO1) or anti-human CD28 as previously described. Trans-CycloOctyne (TCO) – Tetrazine click chemistry was employed to covalently conjugate proteins onto the microbeads. Briefly, 4 million microbeads were resuspended in 800 µl MES buffer containing 200 mM EDC hydrochloride and 200 mM sulfo-NHS for 1h to activate carboxylic groups. Microbeads were then washed with HEPES-CT buffer (HEPES buffer containing 2 mM calcium chloride and 0.5% Tween20) to adjust the pH to 7.2 with a volume of 500 µl. TCO-PEG6-amine (Click Chemistry Tools) was added to the solution to reach a final concentration of 2mM and allowed to conjugate onto the microbeads overnight at room temperature on a roller. The microbeads were dialyzed against HEPES-CT buffer using a 1000 KD dialysis bag (Spectrum Laboratories) to remove excessive TCO (HEPES-CT buffer was replaced 2-3 times per day). Streptavidin (Thermofisher, USA) and anti-CD28 (Biolegend, 302902) antibodies were mixed at a 1:4 molar ratio for antigen-specific T cell activation. The mixture was concentrated in 100 µl HEPES buffer using an Amicon Ultra-2 spin column (Sigma Aldrich, USA). The concentrated mixture was mixed with Tetrazine-PEG5-NHS (Sigma Aldrich, USA) at a molar ratio of 1:5 and reacted for 30 min. The antibody/protein-tetrazine complex was then desalted using a spin column and rinsed with HEPES 5 times to remove unreacted Tetrazine-PEG5-NHS. The purified protein-tetrazine complex was mixed with glycerol at a 1:1 ratio and preserved at -20 ℃. To refine the ligand density of different synthetic cells, we adjusted the dose of the protein-tetrazine for the tetrazine-TCO ligation with TCO-labeled microbeads. HLA-A*02:01 monomer (SLLMWITQV, NIH tetramer) was added to the beads solution at 4 equivilents of streptavidin and 4 hours after the clisk chemistry.

To confirm the conjugation of proteins on the bead surface, Rat anti-human HLA-A,B,C (BioRad), Alexa Fluor™ 647 goat anti-rat IgG, and Alexa Fluor™ 488 goat anti-mouse IgG (Invitrogen) were used to stain the beads. Confocal images were acquired using a Leica SP8-STED confocal microscope and further analyzed using ImageJ software.

Mechanical property and ligand density characterization of synthetic cells

Rheological measurements were performed using an Anton Parr Rheometer. The same formulation as the water phase is used for the fabrication of 8 mm disks of gels of different

viscoelasticity. The disk had an average thickness of about 2 mm. For the formation of an elastic hydrogel, a previously established protocol for elastic beads was followed. Specifically, a 3% VLVG solution was crosslinked with a certain concentration of calcium crosslinker to create an 8 mm gel disk. Gel samples were equilibrated with MES buffer (pH=6) for 1 hour, followed by immersion in an MES solution containing adipic acid dihydrazide (AAD) and hydroxybenzotriazole (HoBt) under constant stirring. This ensured an even distribution of AAD within the alginate matrix. The mixture was left to react at room temperature overnight, allowing the formation of an alginate gel with both ionic and covalent bonds. Subsequently, the gel samples were immersed in a sodium citrate buffer for 2 hours to chelate and remove the calcium ions from the gel. Lastly, the resulting covalent alginate gel was thoroughly rinsed with deionized water and equilibrated in HEPES buffer for 24 hours to ensure the complete removal of unreacted components and stabilization of the gel's mechanical properties.

For the rheological test, an 8-mm PP025 measuring plate was used. The gel samples were carefully placed in the center of the rheometer plate with a spatula. The cantilever was lowered to the preferred gap height (1 mm was used in this study). Oscillatory frequency sweeps (0.1–100 Hz, 1% strain) were conducted at room temperature to measure the storage (G', Pa) and loss (G", Pa) moduli. All experiments were repeated at least three times.

The compressive moduli and stress relaxation properties of the viscoelastic gel were evaluated via compression tests on gel disks (8 mm in diameter, 2 mm thick, equilibrated in RPMI for 24 h) using a method from a previously published study. The gel disks were compressed with a deformation rate of 1/120 mm/s for 30 seconds using a Chatillon TCD225 series force measurement system. The slope of the stress-strain curves (first 5-10% of strain) was used as the initial compressive modulus. Thereafter, the strain was held constant while the load was recorded over time. Stress relaxation was calculated by measuring the time it took for the stress to decrease to half from the maximum stress. No prestress was applied to the gels for these measurements. Compression and stress relaxation measurements of elastic hydrogels were performed using the same procedure.

The average antibody density per synthetic cell was determined by quantitative flow cytometry. Briefly, $1x10^5$ synthetic cells from each experimental group were conjugated with the appropriate antibody: Anti-CD28 FITC (Biolegend 300305). Synthetic cells were then washed and resuspended in HEPES-CT buffer for analysis in a Flow Cytometer (BD LSRFortessa Cell Analyzer). A standard curve was constructed using Quantum Simply Cellular anti-Mouse IgG beads (#815, Bang Laboratories) stained with Anti-CD28 FITC.

AFM for measuring SynVAC-pMHC mechanical properties

Synthetic cells of different viscoelasticity were placed on a JPK NanoWizard 4a BioScience atomic force microscope (AFM) and indented by a Bruker SAA-SPH-1UM probe with a spring constant k = ~0.25 N/m (the exact k value of each probe was determined by LDV calibration and utilized for the specific test). After the force spectroscopies were obtained, Young's modulus was determined by fitting the data to a Hertz/Sneddon model using JPK Data Processing67. To measure viscoelasticity, the height after reaching 10 nN was maintained constantly on the surface of SynVAC-pMHC, and the stress relaxation profile was obtained by recording the vertical deflection force over the relaxation time.

X-ray Photoelectron Spectroscopy (XPS) Analysis for SynVAC-pMHC composition

The SynVAC-pMHC were carefully prepared and mounted for XPS measurements using an Axis Ultra DLD spectrometer (Kratos Analytical Inc.; Chestnut Ridge, NY). The analysis was conducted under ultrahigh vacuum conditions to prevent contamination and interference from atmospheric gases. We used a monochromatic Al Kα X-ray source (λ = 1486.6 eV) for excitation and scanned a wide range of binding energies to capture the complete elemental profile of the bead surfaces. The core level spectra were acquired for Carbon (C 1s) and Calcium (Ca 2p1/2 2p3/2), and the peak areas were integrated to calculate the atomic ratios. The data were analyzed and quantified to determine the concentration of calcium in the beads.

SEM imaging of the interactions between SynVAC-pMHC and ESO-T cells

Donor PBMC samples were assayed for HLA-A*0201 expression via FACS. Human $CD8^+$ T cells were isolated from PBMCs using a human $CD8^+$ T Cell Isolation Kit (Miltenyi Biotec), and ESO-T were sorted using FACS. ESO-T cells were stimulated with FRB for 2 hours and then fixed using 4% glutaraldehyde at 4-degree °C for 2 hours. Subsequent post-fixation with 1% osmium tetroxide was applied for another 2 hours. After fixation, the T cells were rinsed with HEPES-C buffer and then dehydrated through a graduated series of ethanol concentrations (75%, 85%, and 95%), with each step lasting 30 minutes. The samples were then dried using a Tousimis Autosamdri-810 critical point dryer. The specimens were subsequently mounted on specimen stubs and sputter-coated with a gold layer to prepare them for SEM imaging.

***In vitro* antigen-specific T cell expansion**

Donor PBMC samples were assayed for HLA-A*0201 expression via FACS. Human PBMCs were stimulated using FRB, MRB, SRB, or moDCs, respectively. Monocytes were sorted from

PBMCs via the CD14+ microbeads (Miltenyi Biotec). The cells are subsequently cultured for differentiation and maturation using the Mo-DC Generation Toolbox (Miltenyi Biotec). Mature moDCs were pulsed with 10 μg/ml peptide (SLLMWITQV) for 6 h at 37 °C prior to culture. An initial number of 1 x 10^6 PBMCs was seeded in the starting culture media supplied with 100 IU/ml recombinant IL-2 (Biolegend) and activated at a bead-to-cell ratio of 1:1. Fresh media containing 100 IU/ml IL-2 was added to the cells to keep the cell density below 2 x 106 cells/ml throughout the culture process. Cell numbers were counted on day 3, day 7, and day 14. Fold expansion was calculated by dividing the number of cells at the respective time point by the number of cells seeded at the start of the culture.

Flow cytometry analysis of T cells

Cells were harvested at certain time points, and the percentage of ESO-T was evaluated using flow cytometry. All flow cytometry stains were performed in PBS for 30 min on ice. The samples were stained with Human Fc Receptor Blocking Solution (TrueStain FcX) before antibody staining. Antibody staining was performed at a certain dilution according to the manufacturer's instructions. Fluorochrome-conjugated antibodies specific for human CD4 (Clone OKT4), CD8 (Clone SK1), CD3 (Clone HIT3a), CD45RO (Clone UCHL1), CD19 (Clone HIB19), CD69 (Clone FN50), CD45RA (Clone HI100), CD62L (Clone DREG-56), CD95 (Clone G043H7), CD25 (Clone BC96), and streptavidin were purchased from Biolegend. Goat anti-mouse IgG F(ab')2 secondary antibody was purchased from Thermo Fisher. Human Fc Receptor Blocking Solution (TrueStain FcX) was purchased from Biolegend. Intracellular phosphorylation signals were stained using a Cell Fixation/Permeabilization Kit (BD Biosciences). Stained cells were analyzed using LSRII (BD Biosciences). FlowJo v10 software was utilized to analyze the data.

***In vitro* tumor killing assay**

Tumor cells (1×10^4 cells per well) were co-cultured with effector cells (at ratios indicated in figure legends) in T cell culture medium in Corning 96-well clear-bottom black plates for 24 hours. At the end of the culture, live tumor cells were quantified by adding D-luciferin (150 μg/ml; Caliper Life Science) to cell cultures and reading out luciferase activities using an Infinite M1000 microplate reader (Tecan).

Enzyme-linked immunosorbent cytokine assays (ELISA)

The ELISAs for detecting human cytokines were performed following a standard protocol from BD Biosciences. Supernatants from cell culture assays were collected and assayed to quantify human IL-2, TNF-α, and IFN-γ. The capture and biotinylated pairs for detecting cytokines were purchased from BD Biosciences. The streptavidin-HRP conjugate was purchased from Invitrogen. Human cytokine standards were purchased from eBioscience. The samples were analyzed for absorbance at 450 nm using an Infinite M1000 microplate reader (Tecan).

T cell infiltration assay

Tumor micro-organoid was generated by using microfluidic chips with around 20 cells per droplet as described previously [53,54]. The organoids were cultured in complete media for 2 days and then cocultured with the expanded ESO-T cells labeled with Cytolight Rapid Red dye (Sartorius) according to the manufacturer's protocol. Briefly, the dye vial was reconstituted in 20 μL DMSO, followed by a 10-fold dilution in PBS. ESO-T cells were incubated at 37 °C with 5 μL of the diluted dye (final 1:500) in PBS for 25 minutes. After one PBS wash, cells were counted and resuspended in complete medium before being plated with tumor organoids at effector-to-target (E:T) ratios of 5:1 or 10:1. Images were taken at different time points using a Zeiss Axio Observer Z1 inverted fluorescence microscope and analyzed using ImageJ software.

Immunofluorescent visualization of immune synapse formation

The expanded ESO-T cells were frozen in CryoStor® CS5 (STEMCELL technology) for 7 days before being thawed for experiments. The cells were then stimulated for 15-60 minutes before being harvested and adhered to a 12 mm cover glass (Citoglas) that had been pre-treated with Poly-L-Lysine (Sigma). The cells were then fixed with 100% methanol at -20 °C for 5 minutes, followed by blocking with HEPES-C buffer containing 5% donkey serum. The samples were subsequently incubated with primary antibodies against CD3ε (1:400, Abcam, ab52959) for 1h at room temperature. After triple washing with HEPES-CT buffer, the cells were incubated with Alexa Fluor™ 488 goat anti-rabbit IgG and Alexa Fluor™ 647 goat anti-mouse IgG secondary antibody for 1 hour. Nuclei were visualized by staining with 4,6-diamidino-2-phenylindole (DAPI; D3571, Thermo Fisher) at a 1:5000 dilution for 5 minutes. Confocal images were acquired using a Leica SP8-STED confocal microscope and further analyzed using ImageJ software. The recruitment index is calculated by [MFI at the proximal site – background]/[MFI at the distal site − background]

Metabolites panel assay

2×10^6 ESO-T cells activated for 2 days were vacuum filtered onto nylon membranes (0.45 μm). Each filter was submerged cell-side down in 400 μl of precooled extraction solvent (40:40:20 acetonitrile/methanol/water) at −20 °C for 20 minutes. After washing, metabolite extracts were collected, centrifuged at 17,000g, dried under nitrogen gas, and reconstituted in HPLC-grade water (10–15 μl per 10^6 cells).

Cell extracts were analyzed by ultra-HPLC coupled to a Q Exactive Plus mass spectrometer (UHPLC-MS) with electrospray ionization and randomized sample injection. LC separation used an XBridge BEH Amide XP column and a gradient of solvent A (aqueous, pH 9.4) and solvent B (acetonitrile). Two flow paths were operated in tandem, staggered by 20 minutes. The 5μl injection was run at 150μl min^{-1}. The mass spectrometer operated in negative and positive ion modes with a resolution of 140,000 and a scan range of m/z 60–2,000. Data was collected with Xcalibur and analyzed using MAVEN, with identification and integration based on retention times from authenticated standards.

FLIM imaging

Fluorescence lifetime imaging was performed on a Leica STELLARIS 8 Fast Lifetime Contrast (FALCON) inverted microscope (previously Leica SP8 FALCON) equipped with a live-cell workstation (37 °C, 5% CO_2; Tokai Hit, Japan). Instrument response function correction is built into the system design. To validate performance, Coumarin 6 dye was routinely measured before imaging, serving as a standard to confirm accurate lifetime detection at ~2.5 ns on the phasor semicircle. Intracellular NAD(P)H and FAD autofluorescence were excited in two-photon mode at 740 nm. Before imaging, cells were balanced in RPMI 1640 containing 10% FBS for 3 hours to avoid autofluorescence of HEPES. Emission was collected using 460/80 nm (NAD(P)H) and 540/50 nm (FAD) bandpass filters. The laser source (1.8 W) was carefully attenuated to 0.5 mW at the objective lens exit aperture, as measured with a Thorlabs photopower meter, to minimize photobleaching and cell damage. FLIM images were acquired at a pixel size of 284 nm and dwell time of 7.69 μs, with 8× line averaging to improve signal-to-noise ratio.

Confocal and TEM imaging of mitochondria

For confocal imaging, 1×10^6 ESO-T cells activated for 2 days were stained with 0.6 ml of phenol red-free RPMI 1640 (ThermoFisher) containing 50nM MitoTracker Green

(ThermoFisher), 0.5mg/ml Hoechst, and 7.5μM Tetramethylrhodamine, Methyl Ester, Perchlorate (TMRM) (ThermoFisher) for 1h in a cell incubator. Cells were then washed once with PBS and immediately sent to the UCLA Metabolism Core for imaging.

For TEM imaging, 1×10^6 cells activated by SynVAC-pMHC were centrifuged and washed with PBS once. 1 ml PBS containing 2.5% glutaraldehyde and 2% paraformaldehyde was then added to fix cells for 30 mins. Samples were then washed with PBS twice and sent to the UCLA Metabolism Core for subsequent slicing, staining, and imaging.

XFe96 seahorse assay

The ESO-T cells are sorted from the expanded T cell population by FACS, and frozen at -80 C one week before thawing. ESO-T cells are co-cultured with FRB, MRB or SRB for 1 or 2 days before sending them to the UCLA Metabolism Core. The cells were subsequently spun down to a poly-lysine-treated 96-well plate at 300g for 5min, with 2.5×10^5 cells in each well. The culture plate was then introduced in the tray of the Seahorse XFe96 analyzer, and the acquisition program was run. This program includes a step of equilibration followed by basal, post-oligomycin injection, and post-FCCP injection measurements. Each of these three steps comprises three loops of three minutes mixing, two minutes waiting, and three minutes measuring. Data was analyzed through the Wave 2.6.1 Software (Agilent Technologies).

Single-cell RNA and TCR sequencing

T cells activated by SynVAC-pMHC and moDCs were cultured and harvested on day 14 and immediately sent to the UCLA Technology Center for Genomics and Bioinformatics (TCGB) Core for single-cell RNA and TCR sequencing. Sequencing was performed using the 10X Genomics Chromium™ Controller Single Cell Sequencing System, following the manufacturer's instructions and the TCGB Core's standard protocol. Library preparation was carried out with the Illumina TruSeq RNA Sample Prep Kit (Cat#FC-122-1001), and sequencing was conducted on an Illumina NovaSeq system with 150 bp paired-end reads (5,000 reads per cell). Read alignment to the human T cell receptor reference genome (hg38) was performed using CellRanger and CellRanger VDJ, enabling the identification and visualization of alpha and beta chain recombination events in T cells activated by SynVAC-pMHC and moDCs. The processed cell matrix, expression data, and associated metadata have been deposited in the Gene Expression Omnibus (GEO) database.

In vivo anti-tumor efficacy study of ESO-T cells in human OVCAR3 and melanoma xenograft NSG mouse models

The experimental design is illustrated in Figure 6a. Briefly, on day 0, NSG mice were intraperitoneally (i.p.) inoculated with either OVCAR3-FG or A375-FG cells (1 × 10^6 cells per mouse). On day 4, the mice received an intravenous (i.v.) injection of either vehicle control (100 µl PBS per mouse) or ESO-T cells (3 × 10^6 ESO-T cells in 100 µl PBS per mouse). Tumor burden was monitored over time using bioluminescence imaging (BLI). On day 60 (for OVCAR3-FG) or day 32 (for A375-FG), the mice were euthanized, and their tissues were collected for further analysis.

In vivo bioluminescence imaging (BLI)

Bioluminescence imaging was performed using a Spectral Advanced Molecular Imaging (AMI) HTX system (Spectral Instrument Imaging). Live animal imaging was acquired 5 minutes after intraperitoneal (i.p.) injection of D-Luciferin (1 mg/mouse) for total-body bioluminescence and 15 minutes after i.p. injection of D-Luciferin (3 mg/mouse) for tissue-specific bioluminescence. Imaging data were analyzed using AURA imaging software (Spectral Instrument Imaging).

Statistical analysis

Data are presented as mean ± standard deviation (SD). Statistical significance between two groups was determined using a two-tailed Student's t-test in GraphPad Prism 10. For comparisons involving more than two groups, one-way analysis of variance (ANOVA) was performed, followed by Tukey's multiple comparison test. Two-way ANOVA was used to analyze differences among multiple groups with two independent variables. Statistical significance was defined as follows: not significant ($P > 0.05$); *$P < 0.05$; **$P < 0.01$; ***$P < 0.001$.

Supporting information

Supporting Information is available.

Acknowledgments

This work was supported in part by a UCLA Jonsson Comprehensive Cancer Center (JCCC) Seed Grant (to S.L. and L.Y.), a UCLA Broad Stem Cell Research Center (BSCRC) Innovation Award (to S.L.), a grant from the National Institutes of Health (NIH) (GM143485, to S.L.), a Discovery Stage Award from the California Institute for Regenerative Medicine (CIRM)

(DISC2-14169, to S.L.), an Ablon Scholars Award (to L.Y.), a grant from the National Institutes of Health (NIH) (R01CA220012, to K.S.), a USC Ming Hsieh Institute Research Award (to K.S.), a Mann Engineering in Medicine Pilot Grant (to K.S.), a grant from the National Institutes of Health (NIH) (R35GM143127, to J.-O.P.), and a NIH instrumentation grant (1S10OD016387-01, to J.-O.P.). Y.-R.L. is a postdoctoral fellow supported by a UCLA Microbiology, Immunology, and Molecular Genetics M. John Pickett Post-Doctoral Fellow Award and a CIRM-BSCRC Postdoctoral Fellowship. H.Z. is a postdoctoral fellow supported by a CIRM Postdoctoral Fellowship. We thank the UCLA Division of Laboratory Animal Medicine (DLAM) for providing animal support, the UCLA Metabolism core for providing cell metabolism characterization, the UCLA BSCRC Flow Cytometry Core Facility for providing cell sorting support, the UCLA TCGB facility for providing scRNAseq and TCRseq services, the UCLA Center for AIDS Research (CFAR) Virology Core for providing human PBMCs, and the Advanced Light Microscopy/Spectroscopy Laboratory, the Electron Imaging Center for Nanosystems, and the Nano and Pico Characterization Laboratory at the California NanoSystems Institute (CNSI) for supporting the image acquisition. We also thank the NIH Tetramer Facility for providing the peptide-MHC tetramers.

Declaration of interests

L.Y. is a scientific advisor to AlzChem and Amberstone Biosciences, and a co-founder, stockholder, and advisory board member of Appia Bio. None of the declared companies contributed to or directed any of the research reported in this article. The remaining authors declare no competing interests.

Contributions

Y.Y., Z.L., Y.-R.L., L.Y., and S.L. designed the experiments. Y.Y., Y.-R.L., Z.L., H.Z., Y.Z., X.S., D.L., E.M., H.N., B.Z., S.W., J.L., Y.C., B.R., E.Z., J.S. performed the experiments. Y.Y., Y.R.L., Z.L., Y.C., E.Z., and J.S. analyzed the data; Y.Y., Y.-R.L., and Z.L. interpreted the results. Y.Y., Z.L., and Y.L. wrote the original draft. S.L., L.Y., K.S., J.-O.P., J.-J.L., X.S., Z.W., H.Z., Y.Z., X.S., D.L., E.M., H.N., B.Z., S.W., J.L., Y.C., E.Z., and J.S. reviewed and edited the final draft.

Data Availability Statement

All data associated with this study are present in the paper or supplemental information. The genomics data generated during this study are available from the Gene Expression Omnibus

764 database. Any additional information required to reanalyze the data reported in this paper is
765 available from the corresponding authors upon request.
766
767 **References**

768 1. Chandran, S.S., and Klebanoff, C.A. (2019). T cell receptor-based cancer
769 immunotherapy: Emerging efficacy and pathways of resistance. Immunol Rev *290*,
770 127–147. 10.1111/imr.12772.
771 2. Stone, J.D., and Kranz, D.M. (2013). Role of T cell receptor affinity in the efficacy and
772 specificity of adoptive T cell therapies. Front Immunol *4*, 244.
773 10.3389/fimmu.2013.00244.
774 3. Kim, G.B., Fritsche, J., Bunk, S., Mahr, A., Unverdorben, F., Tosh, K., Kong, H.,
775 Maldini, C.R., Lau, C., Srivatsa, S., et al. (2022). Quantitative immunopeptidomics
776 reveals a tumor stroma–specific target for T cell therapy. Science Translational
777 Medicine *14*, eabo6135. doi:10.1126/scitranslmed.abo6135.
778 4. Mazzoccoli, L., and Liu, B. (2024). Dendritic Cells in Shaping Anti-Tumor T Cell
779 Response. Cancers (Basel) *16*. 10.3390/cancers16122211.
780 5. Sabado, R.L., Balan, S., and Bhardwaj, N. (2017). Dendritic cell-based immunotherapy.
781 Cell Research *27*, 74–95. 10.1038/cr.2016.157.
782 6. Li, Y., and Kurlander, R.J. (2010). Comparison of anti-CD3 and anti-CD28-coated beads
783 with soluble anti-CD3 for expanding human T cells: Differing impact on CD8 T cell
784 phenotype and responsiveness to restimulation. Journal of Translational Medicine *8*,
785 104. 10.1186/1479-5876-8-104.
786 7. Mock, U., Nickolay, L., Philip, B., Cheung, G.W., Zhan, H., Johnston, I.C.D., Kaiser,
787 A.D., Peggs, K., Pule, M., Thrasher, A.J., and Qasim, W. (2016). Automated
788 manufacturing of chimeric antigen receptor T cells for adoptive immunotherapy using
789 CliniMACS prodigy. Cytotherapy *18*, 1002–1011. 10.1016/j.jcyt.2016.05.009.
790 8. Oelke, M., Maus, M.V., Didiano, D., June, C.H., Mackensen, A., and Schneck, J.P.
791 (2003). Ex vivo induction and expansion of antigen-specific cytotoxic T cells by HLA-
792 Ig–coated artificial antigen-presenting cells. Nature Medicine *9*, 619–625.
793 10.1038/nm869.
794 9. Wang, H., and Mooney, D.J. (2018). Biomaterial-assisted targeted modulation of
795 immune cells in cancer treatment. Nature Materials *17*, 761–772. 10.1038/s41563-018-
796 0147-9.
797 10. Huse, M. (2025). Mechanoregulation of lymphocyte cytotoxicity. Nature Reviews
798 Immunology. 10.1038/s41577-025-01173-2.
799 11. Zhang, X., Kim, T.-H., Thauland, T.J., Li, H., Majedi, F.S., Ly, C., Gu, Z., Butte, M.J.,
800 Rowat, A.C., and Li, S. (2020). Unraveling the mechanobiology of immune cells.
801 Current Opinion in Biotechnology *66*, 236–245.
802 https://doi.org/10.1016/j.copbio.2020.09.004.
803 12. Adebowale, K., Gong, Z., Hou, J.C., Wisdom, K.M., Garbett, D., Lee, H.-p., Nam, S.,
804 Meyer, T., Odde, D.J., Shenoy, V.B., and Chaudhuri, O. (2021). Enhanced substrate
805 stress relaxation promotes filopodia-mediated cell migration. Nature Materials *20*,
806 1290–1299. 10.1038/s41563-021-00981-w.
807 13. Liu, Y., Blanchfield, L., Ma, V.P.-Y., Andargachew, R., Galior, K., Liu, Z., Evavold, B.,
808 and Salaita, K. (2016). DNA-based nanoparticle tension sensors reveal that T-cell
809 receptors transmit defined pN forces to their antigens for enhanced fidelity. Proceedings
810 of the National Academy of Sciences *113*, 5610–5615. 10.1073/pnas.1600163113.
811 14. Basu, R., Whitlock, B.M., Husson, J., Le Floc'h, A., Jin, W., Oyler-Yaniv, A., Dotiwala,
812 F., Giannone, G., Hivroz, C., Biais, N., et al. (2016). Cytotoxic T Cells Use Mechanical

Force to Potentiate Target Cell Killing. Cell *165*, 100–110. 10.1016/j.cell.2016.01.021.
15. Tello-Lafoz, M., Srpan, K., Sanchez, E.E., Hu, J., Remsik, J., Romin, Y., Calò, A., Hoen, D., Bhanot, U., Morris, L., et al. (2021). Cytotoxic lymphocytes target characteristic biophysical vulnerabilities in cancer. Immunity *54*, 1037–1054.e1037. 10.1016/j.immuni.2021.02.020.
16. Liu, Y., Zhang, T., Zhang, H., Li, J., Zhou, N., Fiskesund, R., Chen, J., Lv, J., Ma, J., Zhang, H., et al. (2021). Cell Softness Prevents Cytolytic T-cell Killing of Tumor-Repopulating Cells. Cancer Res *81*, 476–488. 10.1158/0008-5472.Can-20-2569.
17. Liu, B., Chen, W., Evavold, Brian D., and Zhu, C. (2014). Accumulation of Dynamic Catch Bonds between TCR and Agonist Peptide-MHC Triggers T Cell Signaling. Cell *157*, 357–368. 10.1016/j.cell.2014.02.053.
18. Zhu, C., Chen, W., Lou, J., Rittase, W., and Li, K. (2019). Mechanosensing through immunoreceptors. Nature Immunology *20*, 1269–1278. 10.1038/s41590-019-0491-1.
19. Jeffreys, N., Brockman, J.M., Zhai, Y., Ingber, D.E., and Mooney, D.J. (2024). Mechanical forces amplify TCR mechanotransduction in T cell activation and function. Appl Phys Rev *11*, 011304. 10.1063/5.0166848.
20. Feng, Y., Reinherz, E.L., and Lang, M.J. (2018). αβ T Cell Receptor Mechanosensing Forces out Serial Engagement. Trends Immunol *39*, 596–609. 10.1016/j.it.2018.05.005.
21. Lou, J., Meyer, C., Vitner, E.B., Adu-Berchie, K., Dacus, M.T., Bovone, G., Chen, A., To, T., Weitz, D.A., and Mooney, D.J. (2024). Surface-Functionalized Microgels as Artificial Antigen-Presenting Cells to Regulate Expansion of T Cells. Advanced Materials *36*, 2309860. https://doi.org/10.1002/adma.202309860.
22. Hasani-Sadrabadi, M.M., Majedi, F.S., Zarubova, J., Thauland, T.J., Arumugaswami, V., Hsiai, T.K., Bouchard, L.-S., Butte, M.J., and Li, S. (2024). Harnessing Biomaterials to Amplify Immunity in Aged Mice through T Memory Stem Cells. ACS Nano *18*, 6908–6926. 10.1021/acsnano.3c08559.
23. Yuan, D.J., Shi, L., and Kam, L.C. (2021). Biphasic response of T cell activation to substrate stiffness. Biomaterials *273*, 120797. https://doi.org/10.1016/j.biomaterials.2021.120797.
24. Liu, Z., Li, Y.-R., Yang, Y., Zhu, Y., Yuan, W., Hoffman, T., Wu, Y., Zhu, E., Zarubova, J., Shen, J., et al. (2024). Viscoelastic synthetic antigen-presenting cells for augmenting the potency of cancer therapies. Nature Biomedical Engineering *8*, 1615–1633. 10.1038/s41551-024-01272-w.
25. Adu-Berchie, K., Liu, Y., Zhang, D.K.Y., Freedman, B.R., Brockman, J.M., Vining, K.H., Nerger, B.A., Garmilla, A., and Mooney, D.J. (2023). Generation of functionally distinct T-cell populations by altering the viscoelasticity of their extracellular matrix. Nature Biomedical Engineering *7*, 1374–1391. 10.1038/s41551-023-01052-y.
26. Cribioli, E., Giordano Attianese, G.M.P., Ginefra, P., Signorino-Gelo, A., Vuillefroy de Silly, R., Vannini, N., Hess, C., Irving, M., and Coukos, G. (2022). Enforcing GLUT3 expression in CD8(+) T cells improves fitness and tumor control by promoting glucose uptake and energy storage. Front Immunol *13*, 976628. 10.3389/fimmu.2022.976628.
27. Beumer-Chuwonpad, A., van Alphen, F.P.J., Kragten, N.A.M., Freen-van Heeren, J.J., Rodriguez Gomez, M., Verhoeven, A.J., van den Biggelaar, M., and van Gisbergen, K. (2023). Memory CD8(+) T cells upregulate glycolysis and effector functions under limiting oxygen conditions. Eur J Immunol *53*, e2249918. 10.1002/eji.202249918.
28. Xia, L., Lee, C., and Li, J.J. (2024). Statistical method scDEED for detecting dubious 2D single-cell embeddings and optimizing t-SNE and UMAP hyperparameters. Nature Communications *15*, 1753. 10.1038/s41467-024-45891-y.
29. Subramanian, A., Tamayo, P., Mootha, V.K., Mukherjee, S., Ebert, B.L., Gillette, M.A., Paulovich, A., Pomeroy, S.L., Golub, T.R., Lander, E.S., and Mesirov, J.P. (2005). Gene set enrichment analysis: A knowledge-based approach for interpreting genome-wide

expression profiles. Proceedings of the National Academy of Sciences *102*, 15545–15550. 10.1073/pnas.0506580102.
30. Ashburner, M., Ball, C.A., Blake, J.A., Botstein, D., Butler, H., Cherry, J.M., Davis, A.P., Dolinski, K., Dwight, S.S., Eppig, J.T., et al. (2000). Gene Ontology: tool for the unification of biology. Nature Genetics *25*, 25–29. 10.1038/75556.
31. Aleksander, S.A., Balhoff, J., Carbon, S., Cherry, J.M., Drabkin, H.J., Ebert, D., Feuermann, M., Gaudet, P., Harris, N.L., Hill, D.P., et al. (2023). The Gene Ontology knowledgebase in 2023. Genetics *224*. 10.1093/genetics/iyad031.
32. Dustin, M.L. (2014). The immunological synapse. Cancer Immunol Res *2*, 1023–1033. 10.1158/2326-6066.Cir-14-0161.
33. Grakoui, A., Bromley, S.K., Sumen, C., Davis, M.M., Shaw, A.S., Allen, P.M., and Dustin, M.L. (1999). The Immunological Synapse: A Molecular Machine Controlling T Cell Activation. Science *285*, 221–227. 10.1126/science.285.5425.221.
34. Love, M.I., Huber, W., and Anders, S. (2014). Moderated estimation of fold change and dispersion for RNA-seq data with DESeq2. Genome Biology *15*, 550. 10.1186/s13059-014-0550-8.
35. Ge, X., Chen, Y.E., Song, D., McDermott, M., Woyshner, K., Manousopoulou, A., Wang, N., Li, W., Wang, L.D., and Li, J.J. (2021). Clipper: p-value-free FDR control on high-throughput data from two conditions. Genome Biology *22*, 288. 10.1186/s13059-021-02506-9.
36. Schaefer, C.F., Anthony, K., Krupa, S., Buchoff, J., Day, M., Hannay, T., and Buetow, K.H. (2009). PID: the Pathway Interaction Database. Nucleic Acids Res *37*, D674–679. 10.1093/nar/gkn653.
37. Garçon, F., Patton, D.T., Emery, J.L., Hirsch, E., Rottapel, R., Sasaki, T., and Okkenhaug, K. (2008). CD28 provides T-cell costimulation and enhances PI3K activity at the immune synapse independently of its capacity to interact with the p85/p110 heterodimer. Blood *111*, 1464–1471. 10.1182/blood-2007-08-108050.
38. Colombetti, S., Basso, V., Mueller, D.L., and Mondino, A. (2006). Prolonged TCR/CD28 engagement drives IL-2-independent T cell clonal expansion through signaling mediated by the mammalian target of rapamycin. J Immunol *176*, 2730–2738. 10.4049/jimmunol.176.5.2730.
39. Chen, Y., Xu, Z., Sun, H., Ouyang, X., Han, Y., Yu, H., Wu, N., Xie, Y., and Su, B. (2023). Regulation of CD8+ T memory and exhaustion by the mTOR signals. Cellular & Molecular Immunology *20*, 1023–1039. 10.1038/s41423-023-01064-3.
40. Chi, H. (2012). Regulation and function of mTOR signalling in T cell fate decisions. Nature Reviews Immunology *12*, 325–338. 10.1038/nri3198.
41. Pollizzi, K.N., Waickman, A.T., Patel, C.H., Sun, I.H., and Powell, J.D. (2015). Cellular size as a means of tracking mTOR activity and cell fate of CD4+ T cells upon antigen recognition. PLoS One *10*, e0121710. 10.1371/journal.pone.0121710.
42. Pearce, E.L. (2010). Metabolism in T cell activation and differentiation. Curr Opin Immunol *22*, 314–320. 10.1016/j.coi.2010.01.018.
43. Pham, D.L., Cappabianca, D., Forsberg, M.H., Weaver, C., Mueller, K.P., Tommasi, A., Vidugiriene, J., Lauer, A., Sylvester, K., Lika, J., et al. (2025). Label-free metabolic imaging monitors the fitness of chimeric antigen receptor T cells. Nature Biomedical Engineering. 10.1038/s41551-025-01504-7.
44. Zhou, H., Li, I., Bramlett, C.S., Wang, B., Hao, J., Yen, D.P., Ando, Y., Fraser, S.E., Lu, R., and Shen, K. Label-free metabolic optical biomarkers track stem cell fate transition in real time. Science Advances *10*, eadi6770. 10.1126/sciadv.adi6770.
45. Buck, M.D., O'Sullivan, D., Klein Geltink, R.I., Curtis, J.D., Chang, C.H., Sanin, D.E., Qiu, J., Kretz, O., Braas, D., van der Windt, G.J., et al. (2016). Mitochondrial Dynamics Controls T Cell Fate through Metabolic Programming. Cell *166*, 63–76.

10.1016/j.cell.2016.05.035.
46. Blumenthal, D., Chandra, V., Avery, L., and Burkhardt, J.K. (2020). Mouse T cell priming is enhanced by maturation-dependent stiffening of the dendritic cell cortex. eLife *9*, e55995. 10.7554/eLife.55995.
47. Kornberg, M.D. (2020). The immunologic Warburg effect: Evidence and therapeutic opportunities in autoimmunity. Wiley Interdiscip Rev Syst Biol Med *12*, e1486. 10.1002/wsbm.1486.
48. Bengsch, B., Johnson, A.L., Kurachi, M., Odorizzi, P.M., Pauken, K.E., Attanasio, J., Stelekati, E., McLane, L.M., Paley, M.A., Delgoffe, G.M., and Wherry, E.J. (2016). Bioenergetic Insufficiencies Due to Metabolic Alterations Regulated by the Inhibitory Receptor PD-1 Are an Early Driver of CD8(+) T Cell Exhaustion. Immunity *45*, 358–373. 10.1016/j.immuni.2016.07.008.
49. Ando, S., Perkins, C.M., Sajiki, Y., Chastain, C., Valanparambil, R.M., Wieland, A., Hudson, W.H., Hashimoto, M., Ramalingam, S.S., Freeman, G.J., et al. (2023). mTOR regulates T cell exhaustion and PD-1–targeted immunotherapy response during chronic viral infection. The Journal of Clinical Investigation *133*. 10.1172/JCI160025.
50. Rao, R.R., Li, Q., Odunsi, K., and Shrikant, P.A. (2010). The mTOR Kinase Determines Effector versus Memory CD8+ T Cell Fate by Regulating the Expression of Transcription Factors T-bet and Eomesodermin. Immunity *32*, 67–78. https://doi.org/10.1016/j.immuni.2009.10.010.
51. Pearce, E.L., Walsh, M.C., Cejas, P.J., Harms, G.M., Shen, H., Wang, L.-S., Jones, R.G., and Choi, Y. (2009). Enhancing CD8 T-cell memory by modulating fatty acid metabolism. Nature *460*, 103–107. 10.1038/nature08097.
52. Liu, Z., Li, Y.-R., Yang, Y., Zhu, E., Nan, H., Yan, Y., Zhang, B., Chen, G., Pedroncelli, N., Lyu, Z., et al. (2025). Manufacturing synthetic viscoelastic antigen-presenting cells for immunotherapy. Nature Protocols. 10.1038/s41596-025-01265-2.
53. Ding, S., Hsu, C., Wang, Z., Natesh, N.R., Millen, R., Negrete, M., Giroux, N., Rivera, G.O., Dohlman, A., Bose, S., et al. (2022). Patient-derived micro-organospheres enable clinical precision oncology. Cell Stem Cell *29*, 905–917.e906. 10.1016/j.stem.2022.04.006.
54. Wang, Z., Boretto, M., Millen, R., Natesh, N., Reckzeh, E.S., Hsu, C., Negrete, M., Yao, H., Quayle, W., Heaton, B.E., et al. (2022). Rapid tissue prototyping with micro-organospheres. Stem Cell Reports *17*, 1959–1975. https://doi.org/10.1016/j.stemcr.2022.07.016.

Figures

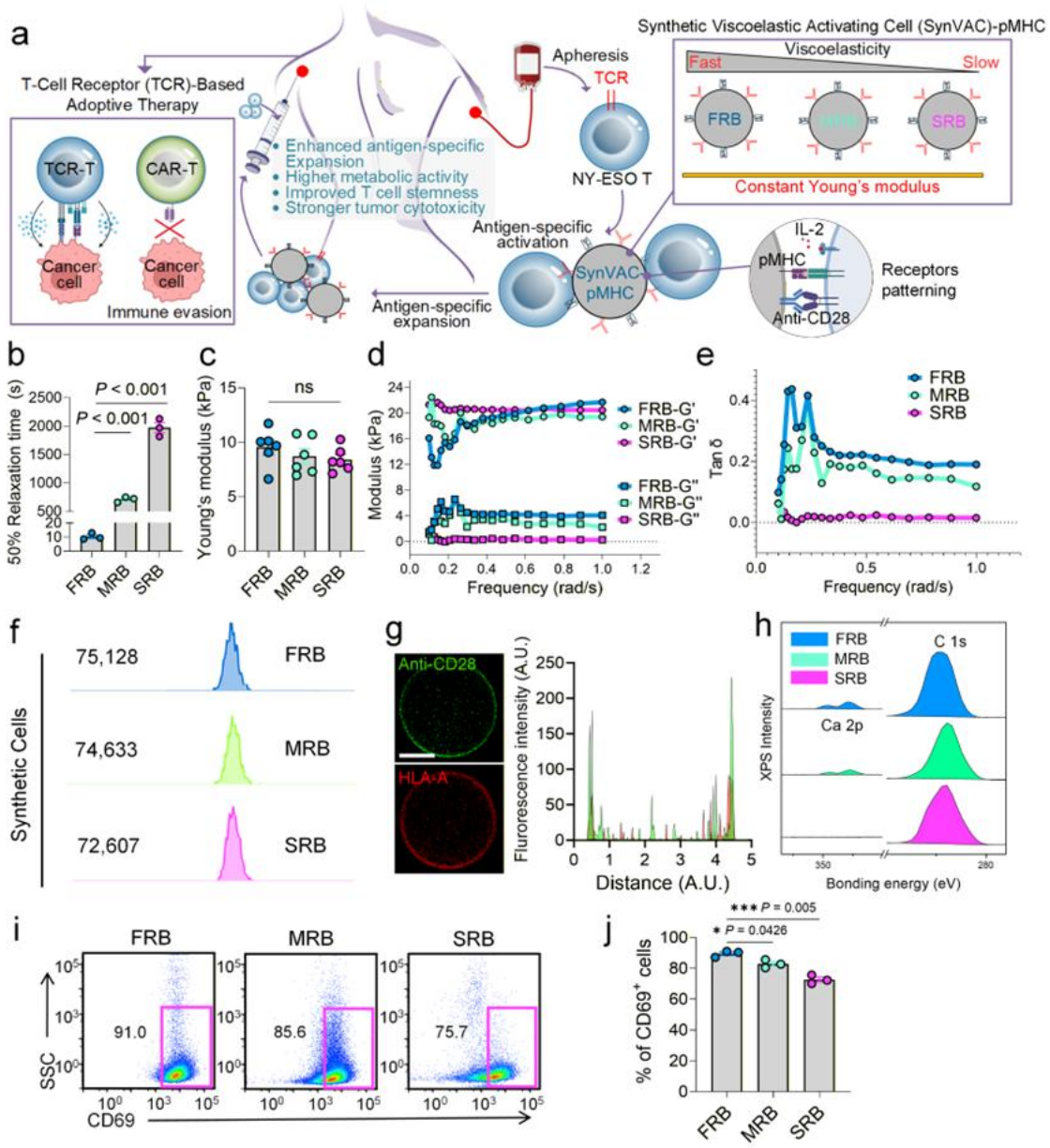


Figure 1. Mechanical characterization and ligand presentation of SynVAC-pMHC.

a, Schematic showing clinical procedures of TCR-T cell expansion for cancer therapy. The panel at top right shows that SynVAC-pMHC can be fabricated with a constant Young's modulus but different viscoelasticity as characterized by stress relaxation time: fast-relaxing bead (FRB), medium-relaxing bead (MRB), and slow-relaxing bead (SRB). The surface of SynVAC-pMHC is functionalized with peptide-MHC tetramer complex and anti-CD28, mimicking natural APCs to enhance TCR-T cell expansion with higher metabolic activity and stemness.

b-c, Compressive testing confirms matched stiffness but distinct half stress-relaxation times across SynVAC-pMHC. (N = 3).

d-e, Rheometry validates increased loss modulus (G″) and tan δ in FRBs, indicating enhanced viscoelasticity, representative of 3 independent experiments.

f, Flow cytometry analysis of SynVAC-pMHC of different viscoelasticity confirms the equal ligand density, representative of 3 independent experiments.

g, Confocal imaging of FRB showing the peptide-MHC and anti-CD28 are coated on the surface of the microbeads, representative of 3 independent experiments.

h, X-ray photoelectron spectroscopy (XPS) revealed FRB and MRB are ionically crosslinked with calcium ions, while SRB is covalently crosslinked, representative of 3 independent experiments.

i-j, Flow cytometry analysis of the CD69 expression of the SynVAC-pMHC cocultured with sorted ESO-T cells for 48 hours (n = 4), which indicates that high viscoelasticity SynVAC-pMHC better activates ESO-T cells at the early time point.

In **b**, **c, j**, data represent mean ± s.e.m.**,** and significance was determined by a one-way ANOVA. (ns, not significant, *P<0.05, **P<0.01, ***P<0.001).

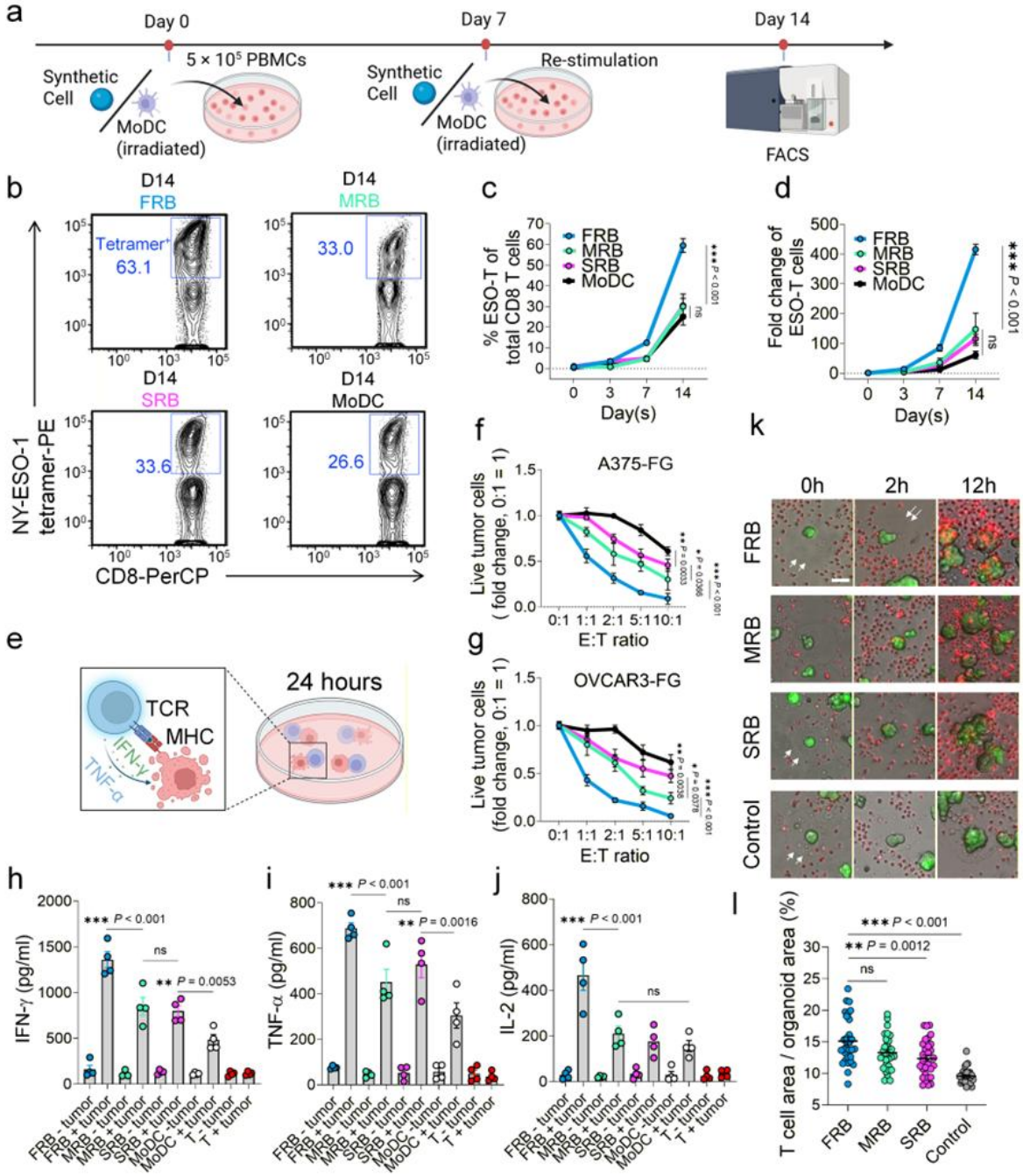


Figure 2. *In vitro* expansion and functional characterization of TCR-T cells by SynVAC-pMHC.

a, Experimental workflow: PBMCs were stimulated with irradiated moDCs or SynVAC-pMHC (FRB, MRB, or SRB) at day 0 with restimulation on day 7. The media was changed 2 days after the addition of SynVAC-pMHC to remove the synthetic cells. The cell culture at day 14 was used for the following FACS analysis.

b, Representative flow cytometry analysis of the ESO-T percentage of cells expanded by different SynVAC-pMHC or moDCs.

c-d, SynVAC-pMHC, particularly FRBs, promoted stronger expansion of ESO-T cells over time, as measured by tetramer staining and cell number measurement (N = 3).

e, Schematic representation of the *in vitro* tumor killing assay, where T cells and tumor cells were cocultured for 24 hours.

f–g, FRB-expanded ESO-T cells demonstrated superior tumor killing against ESO-T cell + A375-FG (melanoma) and OVCAR3-FG (ovarian) tumor targets across multiple effector-to-target (E:T) ratios (N = 4).

h–j, Cytokine analysis showed enhanced IFN-γ, TNF-α, and IL-2 production from FRB-stimulated ESO-T cells following co-culture with tumor cells (N = 4).

k, Representative images of A375-FG tumor organoid cocultured with ESO-T cells at 0h, 2h, and 12h. E:T ratio = 5:1. Scale bar, 70μm.

l, Quantitative analysis of the organoid infiltration index, which is calculated by the area of T cells in an organoid divided by the area of the organoid, representative of 3 independent experiments.

In **c**–**d, f-j**, data represent mean ± s.e.m.**,** and significance was determined by two-way ANOVA (**c-d**) or one-way ANOVA (**f-j**) (ns, not significant, *P<0.05, **P<0.01, ***P<0.001).

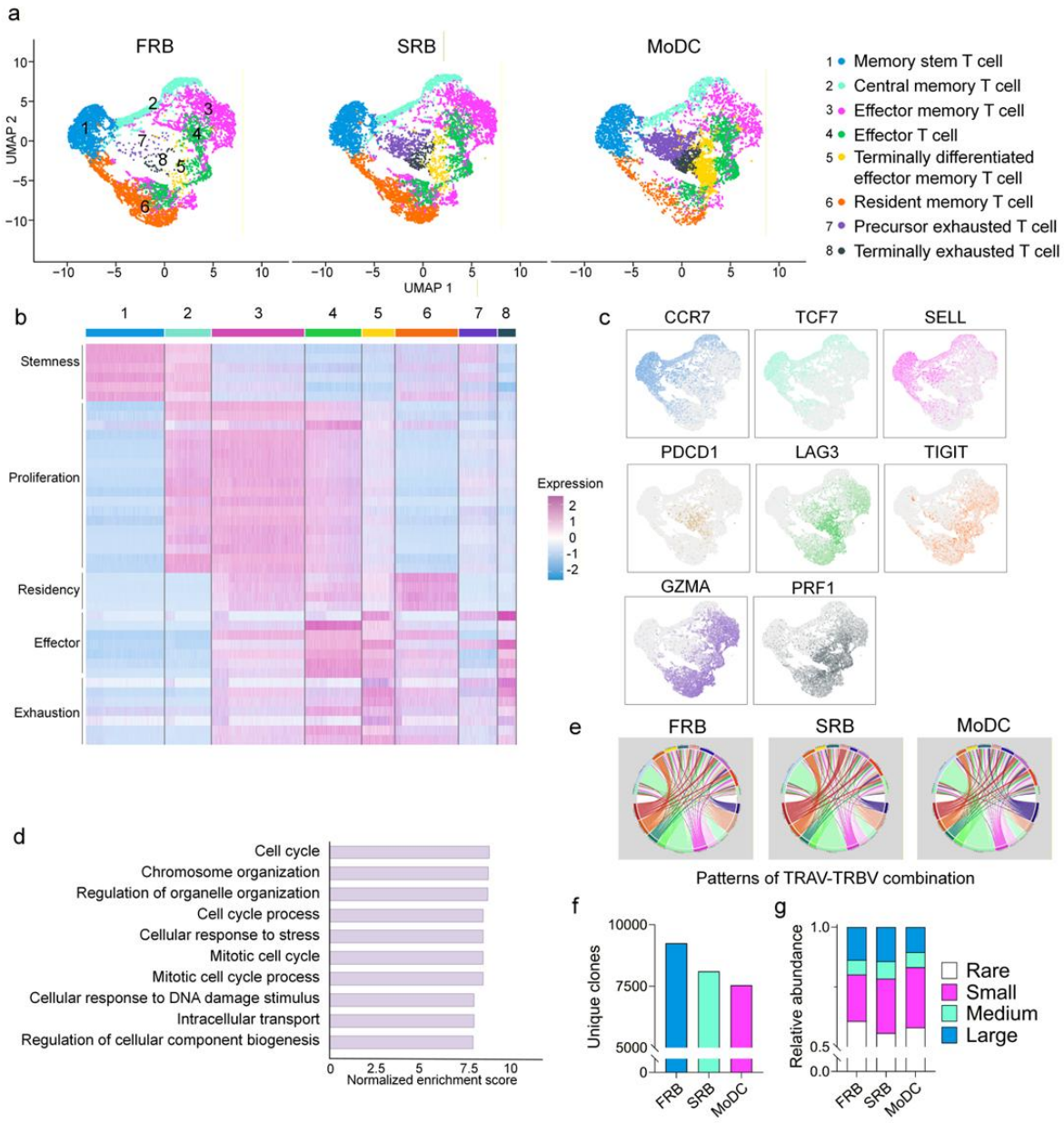


Figure 3. Single-cell RNA sequencing analysis of ESO-T cells expanded by SynVAC-pMHC or moDCs at Day 14.

a, UMAP clustering of ESO-T cells identifies distinct functional populations, including memory stem T cell, central memory T cell, effector memory T cell, effector T cell, terminally differentiated T cell, resident memory T cell, precursor exhausted T cell, and terminally exhausted T cell.

b, Gene lists that are used to identify different clusters in **a**, including stemness, proliferation, residency, effector, and exhaustion.

c, Expression patterns of stemness marker genes (CCR7, TCF7, SELL), exhaustion marker genes (PDCD1, LAG3, TIGIT), and effector marker genes (GZMA, and PRF1) projected onto UMAP space, highlighting transcriptional features that define distinct T cell subsets.

d, Gene set enrichment analysis (GSEA) of the FRB group using the Gene Ontology Biological Process (GOBP) database, highlighting pathways related to cell division significantly upregulated in the FRB-expanded ESO-T cells.

e, Circos plots depicting TRAV–TRBV pairing frequencies in T cells from FRB-, SRB-, and moDC-activated cells, illustrating distinct V gene usage patterns across activation conditions.
f, Quantification of unique TCR clones detected in each condition
g, Distribution of TCR clone sizes categorized as rare (X <= 0.01%), small (0.1% < X <= 1%), medium (1% < X <= 10%), or large (10% < X), showing differences in clonal expansion dynamics.

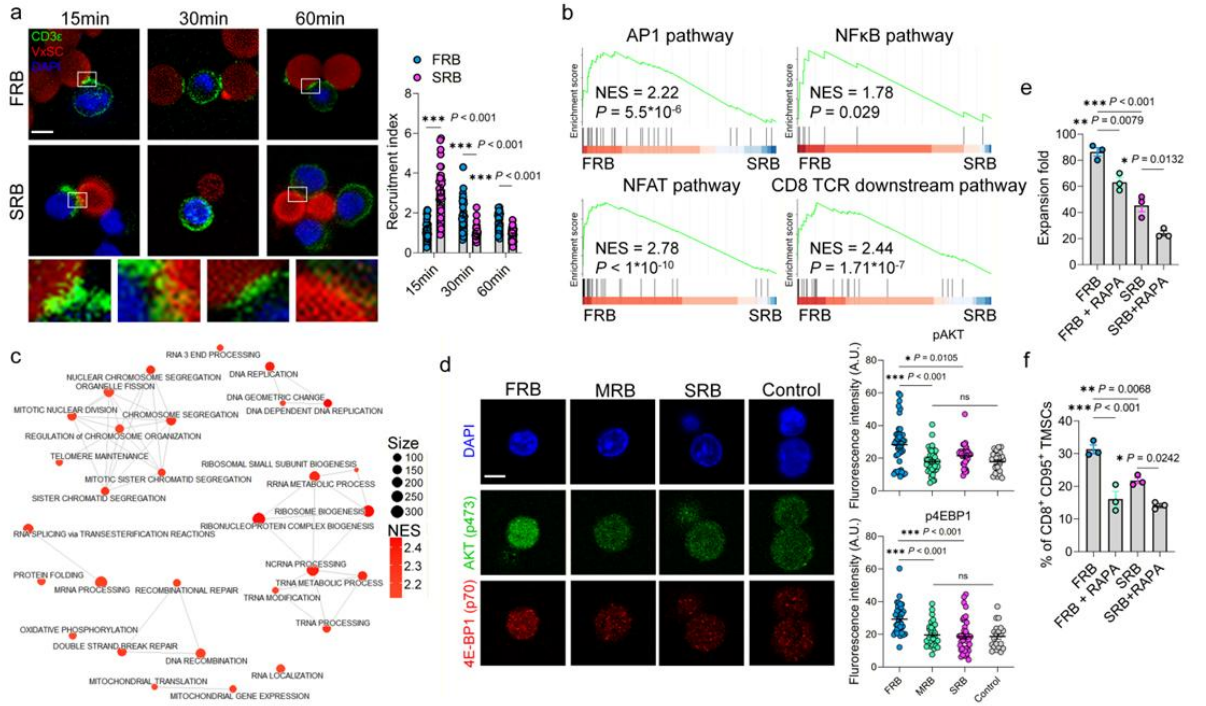


Figure 4. FRB induces stronger early T cell activation signals and enhances expansion and TMSC formation mediated by the mTOR pathway.
a, Confocal imaging of ESO-T cells forming immunological synapses with FRB or SRB at 15min, 30 min, and 60 min post-activation. FRB showed stronger interaction with ESO-T cells as evidenced by a higher CD3e recruitment index (N = 10). Representative of 3 independent experiments. Scale bar: 5 μm.
b, Gene set enrichment analysis (GSEA) result of bulk RNA sequencing data from FRB and SRB-activated ESO-T cells at 6 hours post-activation (N = 4), showing enhanced early T cell activation signals in the FRB group. The PID dataset from the Molecular Signatures Database was used for GSEA.
c, Enrichment Map plot of bulk RNA sequencing data from FRB and SRB-activated ESO-T cells at 24 hours post-activation (N = 4), showing enhanced cell division and metabolism in the FRB group. Normalized enrichment score (NES) was calculated using GSEA of the gene ontology: biological process (GO: BP) dataset from the Molecular Signatures Database.
d, Confocal imaging of the phosphorylated AKT and 4E-BP1 in ESO-T cells activated for 1 hour, which are downstream targets of mTORc2 and mTORc1, respectively, showing enhanced mTOR signals for the FRB group. Scale bar: 5 μm. Representative of 3 independent experiments.
e, The expansion fold of ESO-T cells cocultured with FRB or SRB with or without the addition of 100nM rapamycin (RAPA) during the coculture period, which shows that mTOR signaling is involved in T cell proliferation. Representative of 3 independent experiments.

f, The T memory stem cell (TMSC) percentage of ESO-T cells cocultured with FRB or SRB in the absence or presence of 100nM rapamycin (RAPA) during the coculture period, which shows the role of mTOR signaling in TMSC generation. Representative of 3 independent experiments. In **a**, **d**-**f**, data represent mean ± s.e.m.**,** and significance was determined by one-way ANOVA. (NS, not significant, *P<0.05, **P<0.01, ***P<0.001)

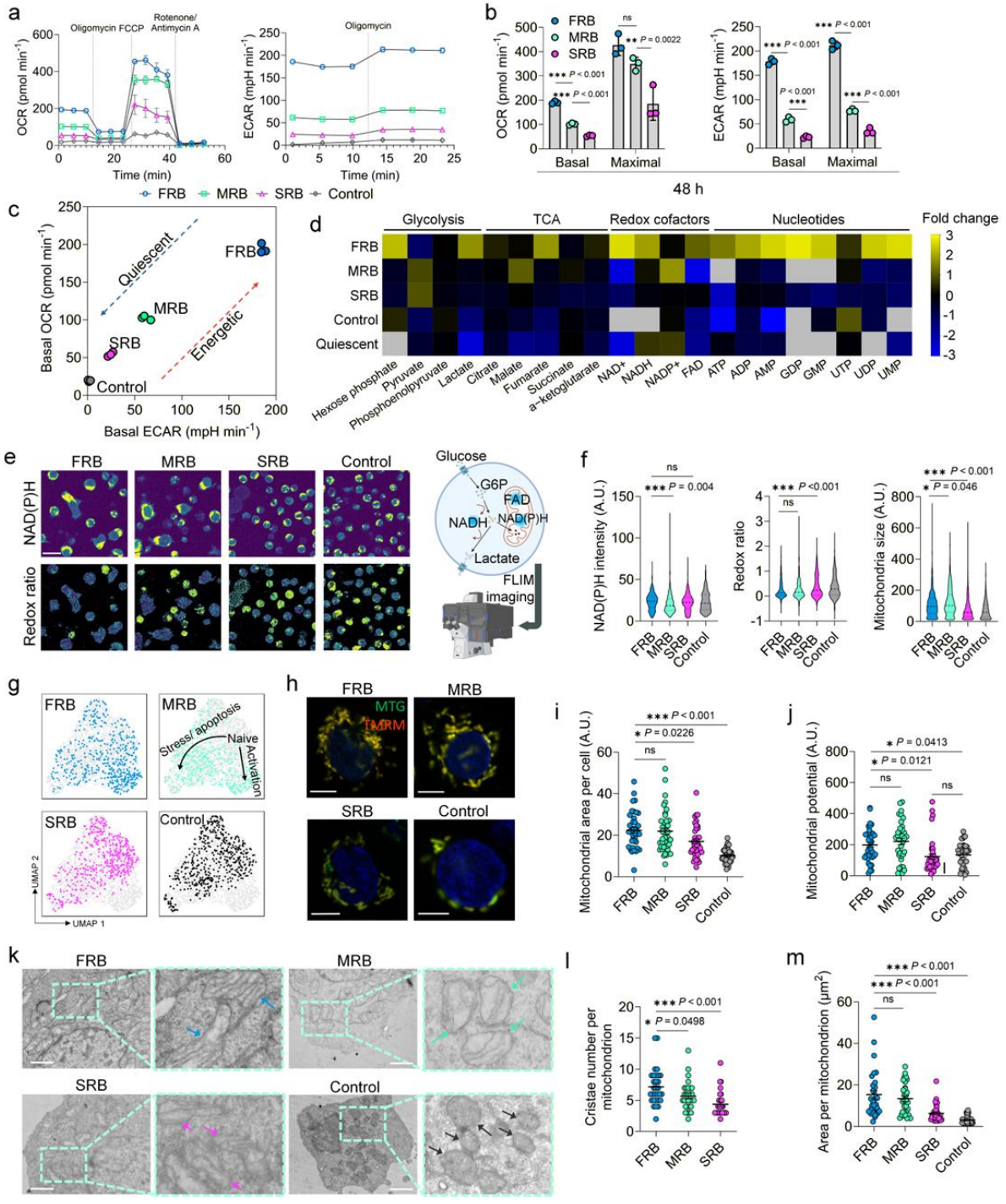


Figure 5. FRB promotes early metabolic activation in ESO-T cells.

a, Seahorse analysis of oxygen consumption rate (OCR, left) and extracellular acidification rate (ECAR, right) in ESO-T cells 48 h after activation by FRB, MRB, or SRB (N = 3).

b, Quantification of basal and maximal OCR (left) and ECAR (right) showing enhanced mitochondrial respiration and glycolytic activity in FRB-stimulated cells (N = 3).

c, Basal OCR and ECAR of ESO-T cells expanded by different SynVAC-pMHC, showing a more energetic metabolic profile of the FRB-activated ESO-T cells (N = 3).
d, Heatmap showing the fold change of key intracellular metabolites, grouped by pathway (Glycolysis, TCA Cycle, Redox cofactors, Nucleotides), comparing FRB, MRB, SRB, Control (IL-2 only), and Quiescent groups. Fold change is calculated by dividing the raw value by the row-wise mean.
e, Fluorescence Lifetime Imaging Microscopy (FLIM) images of ESO-T cells activated by different SynVAC-pMHC. Redox ratio is calculated by the fluorescent intensity of FAD/the fluorescent intensity of NADPH. Representative of 3 independent experiments. Scale bar: 20 μm.
f, Quantification of **e** and mitochondrial size, showing FRB promotes NADPH generation and mitochondrial size growth.
g, 2D metabolic state mapping of individual cells using FLIM-derived features shows distinct clustering of FRB-stimulated cells in an activated metabolic region, while SRB and control groups remain in lower-activity regions. The schematic on the right shows the mechanism of FLIM imaging, where the autofluorescence and fluorescence lifetime of FAD and NAD(P)H are detected by the microscope.
h, Representative confocal imaging of mitochondria structure (Mitotracker Green) and mitochondrial potential (Tetramethylrhodamine methyl ester [TMRM]) staining. Scale bar: 5 μm. Representative of 3 independent experiments.
i, Quantification of mitochondrial area per cell in **h**.
j, Quantification of mitochondrial potential in **h**.
k, Representative images acquired by transmission electron microscope (TEM) of ESO-T cells activated by FRB, MRB, SRB, and control. Arrows indicate mitochondria.
l, Quantification of the cristae number per mitochondrion
m, Quantification of the mitochondria size
In **b, f, i-j**, **l-m**, data represent mean ± s.e.m.**,** and significance was determined by a one-way ANOVA. (ns, not significant, *P<0.05, **P<0.01, ***P<0.001).

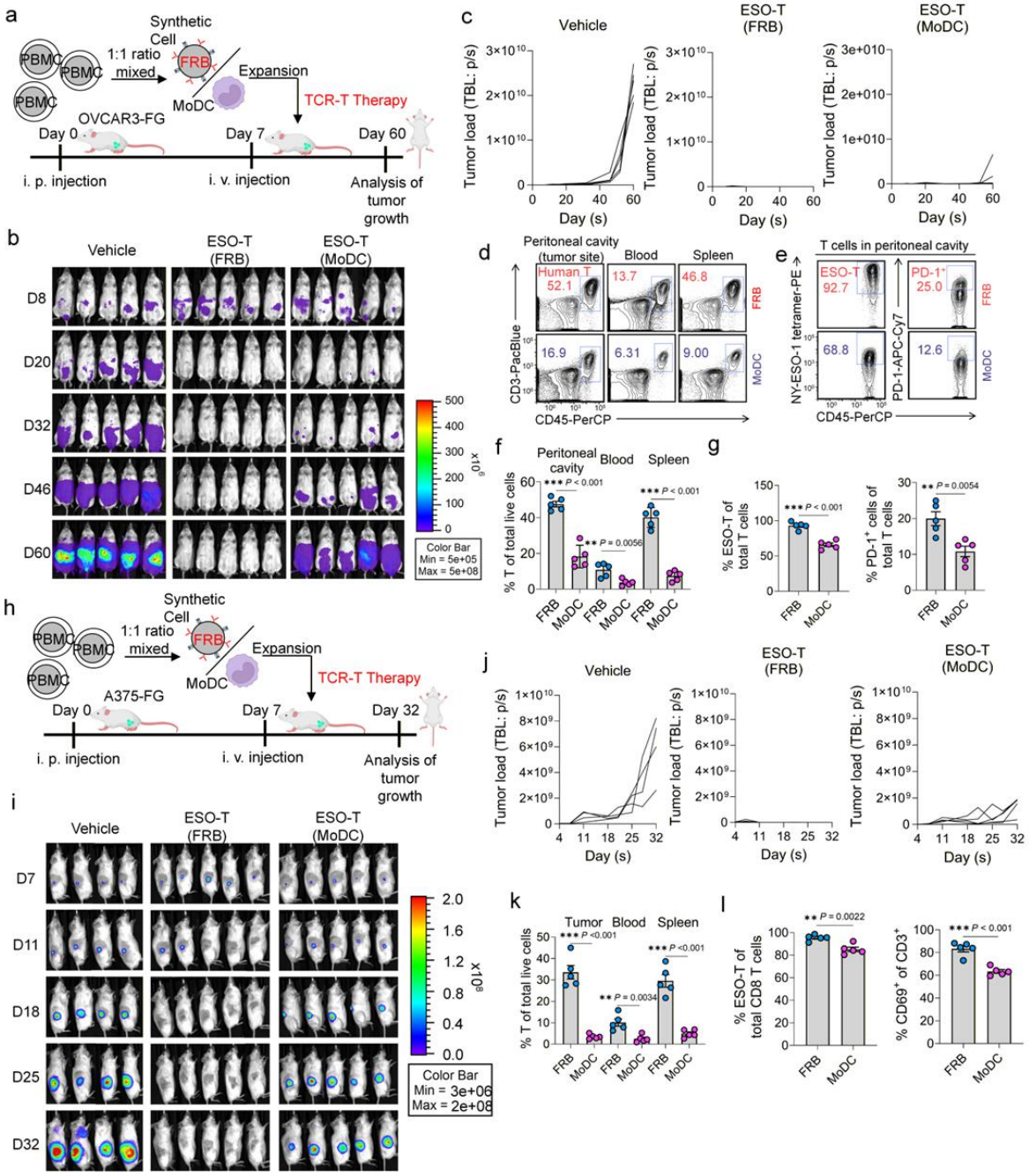


Figure 6. SynVAC-pMHC-expanded TCR-T cells exhibit enhanced antitumor efficacy and persistence in an ovarian cancer model and a melanoma model.

a, Experimental design of the ovarian cancer model.

b, BLI images showing the presence of ovarian cancer cells in experimental mice over time.

c, Quantification of **b** (n = 5).

d, Representative flow cytometry results of the frequency of human T cells in the peritoneal cavity, blood, and spleen at day 60. (n = 5).

e, Representative flow cytometry results of the frequency of ESO-T cells and PD-1$^+$ T cells in the peritoneal cavity at day 60. (n = 5).

f, Quantification of **d** (n = 5).

g, Quantification of **e** (n = 5).

h, Experimental design of the melanoma model.

i, BLI images showing the presence of melanoma cells in experimental mice over time.
j, Quantification of **i** (n = 5)
k, The frequency of human T cells in the tumor, blood, and spleen on day 32 (n = 5).
l, The frequency of ESO-T cells and $CD69^+$ T cells in the tumor on day 32 (n = 5).
In **f–g**, **k-l**, data represent mean ± s.e.m.**,** and significance was determined by Student's t-test. (ns, not significant, *P<0.05, **P<0.01, ***P<0.001)

Extended Figure 1. Characterization of SynVAC-pMHC with various relaxation times, expansion efficiency, and *in vitro* tumor-killing efficacy.
a, Relaxation time (50% relaxation time, s) for SynVAC-pMHC (V1, V2, V3, and V4), demonstrating their distinct viscoelastic properties.
b, Representative force relaxation curves over time (s) for each SynVAC-pMHC (V1-V4) measured via atomic force microscopy (AFM), with an inset illustrating the setup.
c, Young's modulus (kPa) for the V1-V4, indicating similar stiffness despite varying relaxation times.
d, Percentage of ESO-T of total CD8 T cells (%) cultured with V1-V4 over 14 days.
e, Fold change of ESO-T cells cultured with V1-V4 over 14 days, relative to Day 0.
f-g, Tumor cell killing efficiency assays: Fold change of live OVCAR3-FG (f) and A375-FG (g) tumor cells after 24 hours of co-culture with ESO-T cells at varying Effector: Target (E: T) ratios (0:1 to 10:1).
In **a**, **c, d-g**, data represent mean ± s.e.m.**,** and significance was determined by two-way ANOVA (**d-g**) or one-way ANOVA (**a**, **c**) (ns, not significant, *P<0.05, **P<0.01, ***P<0.001).

Extended Figure 2. Gene Set Enrichment Analysis (GSEA) of cells activated by FRB and SRB at Day 14.
a, Bar plot showing the Normalized Enrichment Scores (NES) for the top pathways identified by comparing cells cultured with the FRB against the SRB using the single-cell RNA sequencing result. The Pathway Interaction Database was used for analysis.
b-c, Gene sets enrichment plots for selected pathways. The green curve represents the running enrichment score. Positive indicates enrichment in the FRB group, and negative indicates enrichment in the SRB group. Corresponding and values are displayed for: Oxidative phosphorylation (b), Glycolysis (c). The hallmark gene sets were used for the analysis of b-c.

Extended Figure 3. Molecular profiling of $CD8^+$ T cells cultured with FRB or SRB.
a, Western blotting analysis at 1 hour post-activation showing phosphorylation or expression of signaling proteins: pIκBα, IκBα, pNF-κB (p65), p-c-Jun, c-Jun, in CD8 T cells cultured on FRB and SRB substrates. Molecular weights (kDa) are indicated. Left to right: Control, SRB, and FRB.
b, Principal Component Analysis (PCA) plots of gene expression data for ESO-T cells cultured with FRB, SRB, and Control group, analyzed at 6 hours (left) and 24 hours (right).
c-d, Heatmaps of the top 100 upregulated and downregulated genes in ESO-T cells cultured on FRB vs. SRB at 6 hours (c) and 24 hours (d), relative to the Control condition. The z-score is indicated by the color scale.
e, GSEA enrichment plots at 6 hours for the HIF1 binding site V$HIF1_Q5 (left) and FOXO1 binding site V$FOXO1_01 (right), showing enrichment for mTORc1 and mTORc2 downstream targets.

f, GSEA enrichment plots at 24 hours for Glycolysis (left) and Oxidative phosphorylation (right) pathways comparing FRB vs. SRB. NES and P values are shown.
g, Bar plot showing the Normalized Enrichment Score for the top Hallmark pathways enriched at 24 hours using the Pathway Interaction Database (PID) gene sets.
h, Mean Fluorescence Intensity (MFI) of total pAKT and pS6BP1 in ESO-T cells cultured with FRB and with and without Rapamycin (RAPA) treatment, showing decreased mTORc2 and mTORc2 activity, respectively.
i, Metabolic analysis of CD8 T cells: Oxygen Consumption Rate (OCR) and Extracellular Acidification Rate (ECAR) over time, with sequential addition of Oligomycin, FCCP, and Rotenone/Antimycin A. Cells are cultured with FRB, MRB, SRB, and FRB+RAPA. This indicates RAPA decreases metabolism in FRB-activated ESO-T cells.
In **h**, data represent mean ± s.e.m.**,** and significance was determined by one-way ANOVA (ns, not significant, *P<0.05, **P<0.01, ***P<0.001).

Extended Figure 4. Metabolic profiling of CD8$^+$ T cells cultured with FRB, MRB or SRB.
ESO-T cells were activated with SynVAC-pMHC for 48 hours, and then used for the following analysis.
a, Histograms showing the distribution of cell diameters (μm) for CD8$^+$ T cells activated by FRB, MRB, and SRB.
b-c, Metabolic analysis of ESO-T cells from two different donors (Donor 2 in b, Donor 3 in c): Oxygen Consumption Rate (OCR) and Extracellular Acidification Rate (ECAR) over time, with sequential addition of Oligomycin, FCCP, and Rotenone/Antimycin A. Cells are cultured with FRB, MRB, SRB, or IL-2 only (Control).
d, Quantification of normalized OCR (Basal and Maximal) and ECAR (Basal and Maximal) derived from the metabolic assays in (b) and (c).
e, Quantification of intracellular lactate and other key intracellular metabolites by pathway (TCA Cycle, cofactors, nucleotides), comparing FRB, MRB, SRB, and Control groups. The score is calculated by averaging the normalized value
f, Violin plots comparing Cell size (A.U.), Circularity, α-bound, and t-bound parameters from FLIM results for ESO-T cells cultured with FRB, MRB, SRB, and IL-2 only (Control).
g, UMAP plots for ESO-T cells, visualizing the distribution of the different cell groups (FRB, MRB, SRB, Control), along with overlayed single-cell characteristics: Cell status (with an arrow indicating the Cell spread population), Cell size, Circularity, NAD(P)H intensity, Redox ratio, α-bound, t-bound, Mitochondria size, and Normalized mitochondria size (i.e. mitochondria size/cell size). The plots are created with results from the FLIM.
In **d**, **e**, **f**, data represent mean ± s.e.m.**,** and significance was determined by one-way ANOVA (ns, not significant, *P<0.05, **P<0.01, ***P<0.001).

Supplementary Files

This is a list of supplementary files associated with this preprint. Click to download.

- Supplementaryinformation.docx
- ExtendedFig.1.png
- ExtendedFig.2.png
- ExtendedFig.3.png
- ExtendedFig.4.png